

Mass transport and surface reactions in microfluidic systems

Thomas Gervais^a, Klavs F. Jensen^{b,*}

^aDivision of Biological Engineering, Department of Chemical Engineering, Massachusetts Institute of Technology, Cambridge, MA 02139, USA

^bDepartment of Chemical Engineering, Massachusetts Institute of Technology, Cambridge, MA 02139, USA

Received 3 May 2005; received in revised form 24 June 2005; accepted 27 June 2005

Available online 19 September 2005

Abstract

We provide analysis of different regimes of diffusion and laminar flow convection combined with bimolecular surface reactions relevant to biochemical assays performed in microfluidic devices. Analytic solutions for concentration fields are compared to predictions from two-dimensional finite element simulations for the various operation regimes. The analytic and numerical results extend the transport models beyond the models commonly used to interpret results from surface plasmon resonance (SPR) experiments. Particular emphasis is placed on the characterization of transport in shallow microfluidic channels in which the fully developed transport regime dominates rather than the mass transfer boundary layer transport typically encountered in SPR. Under fast reaction and diffusion conditions, the surfaces saturate following moving front kinetics similar to that observed in chromatographic columns. Two key parameters relevant to on-chip biochemical assays and microfluidic sensors are studied and compiled: the capture fraction of the bulk analyte at the surface and the saturation time scale of the reactive surfaces. The physical processes in the different regimes are illustrated with data from the relevant microfluidics literature. © 2005 Elsevier Ltd. All rights reserved.

Keywords: Microfluidics; Biochemical engineering; Mass transfer; Mathematical modeling; Adsorption; Graetz problem

1. Introduction

Mass transfer over reactive surfaces in microfluidic devices is central to exploring and quantifying biochemical reactions, such as DNA hybridization and antigen-antibody binding. The small length scales lead to laminar flows (Stone and Kim, 2001; Stone et al., 2004) and the corresponding high surface-to-volume ratio implies that understanding transport and reactions at surfaces requires special consideration. Many applications depend on the accurate prediction of cell–cell, protein–cell or protein–protein interaction at interfaces. Examples include controlling surface passivation (Green et al., 1999), understanding cell attachment and release from surfaces (Lu et al., 2004) and performing general biochemical assays for sensing applications (Auroux et al., 2002). The surface plasmon resonance (SPR)

sensor (Biacore, Uppsala, Sweden) (Fig. 1A) represents an example of surface-based detection systems that monitor adsorption of biological molecules onto the surface of a gold film (Brockman et al., 2000; Malmqvist, 1993; Schuck, 1997). High frequency quartz microbalances (Fig. 1B) have also been used in similar adsorption studies (Okahata et al., 1998). Hollow cantilever-based biosensors (Fig. 1C) are also developed as techniques for measuring adsorption kinetics (Burg and Manalis, 2003). Other chip-based detection systems include fluorescence immunoassays and DNA hybridization on patterned surfaces, either based on soft lithography microfabrication (Bernard et al., 2001) or spotting techniques (MacBeath and Schreiber, 2000; Nielsen et al., 2003). These devices share the common features of a flow-through channel with reactive surfaces (Fig. 1D). In all cases, the sample to be analyzed is directed to the sensor element (the reactive surface) by a convective flow and analytes diffuse to binding sites on the surface.

The steady-state diffusion-limited transport to a surface in a pressure-driven flow is known as the Graetz Problem

* Corresponding author. Tel.: +1 617 253 4589; fax: +1 617 258 8224.
E-mail address: kfjensen@mit.edu (K.F. Jensen).

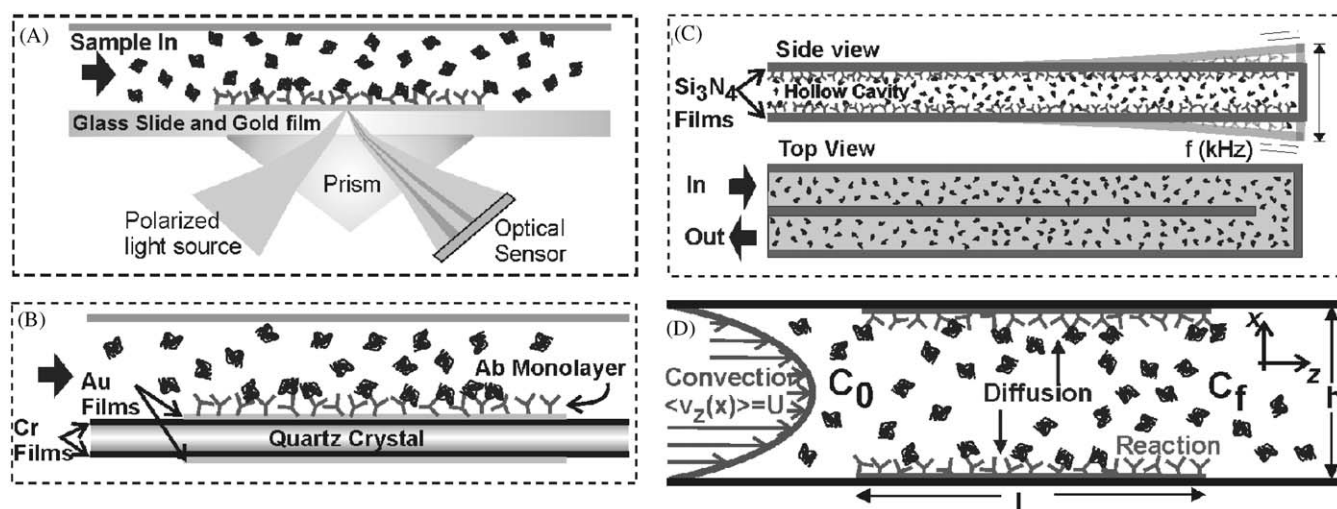


Fig. 1. Microfluidic applications involving convection, diffusion and surface reaction in a flat plate geometry under fully developed parabolic flow conditions. (A) Surface plasmon resonance (SPR) optical sensor (Biacore Inc.). (B) Quartz Crystal Microbalance (QCM). (C) Suspended Microresonator (Hollow Cantilever). (D) General schematics describing the transport to surface in microdevices. The initial concentration of sample before the reaction patch is given to be C_0 and the final, well-mixed concentration is C_f . The capture fraction of the analyte passing over is thus given by $f(L, t) = 1 - C_f(L, t)/C_0$. Asymmetric reactions (as for A and B) involve a reaction at the bottom wall only, while symmetric reactions (as in C) involve an identical reaction at both top and bottom walls.

and it is usually divided into two main operation regimes: the “entrance region” implying the presence of a mass transfer boundary layer¹ and the “fully developed region”, with bulk depletion of the sample (Deen, 1998). In the context of microfluidic systems, the entrance region has been studied in greater details since it is relevant to most SPR systems (Christensen, 1997; Glaser, 1993; Goldstein et al., 1999). Two-compartment models, approximating the mass transfer in the entrance region, have provided additional insight into transport in SPR systems by taking into account surface saturation over time and reaction-limited conditions (Myszka et al., 1998; Vijayendran and Leckband, 2001). With the increasing computing power available, the simplified numerical approach represented by two-compartment models is being replaced by detailed finite element simulations of the complete transport equations.

From a practical point of view, operating a device in the entrance regime, as is often done in SPR, leads to low sample capture fractions. For example, in a typical SPR experiment operating in the boundary regime with a flow of $5 \mu\text{l}/\text{min}$ through a channel of cross-section $50 \times 500 \mu\text{m}^2$ over a 1 mm detection zone, the capture fraction f , i.e., the total mass fraction of a specific bulk protein captured at the surface, is estimated to be 7% under diffusion limiting conditions. The remaining 93% of the analyte mass flows above the capture region and is lost for detection purposes. In this regime, f is expected to vary with the flow rate Q as $f \sim Q^{-2/3}$ (Lok et

al., 1983). Thus, as the fluid velocity increases, more sample needs to be consumed in order to obtain a sufficient signal-to-noise ratio, and consequently, more material is lost in the medium. In general, microfluidic devices aim to minimize sample consumption, yet operating in the entrance region goes against this goal. However, when channels reach the micron scale and the regime switches to “fully developed”, the capture fraction becomes much higher, thus minimizing the detection losses.

The standard entrance region model provides poor estimates for intermediate to high capture fractions. High capture fractions are likely to be needed when expensive or short (small) plug-like samples are to be used. These samples can come from discrete sources, such as a single cell analysis device (Huang et al., 2004), or a sample released from a picoliter compartment (Thorsen et al., 2002) to a detection surface. In these circumstances, the models developed for standard SPR are not appropriate. Laminar flow transport models are needed to describe systems with channel widths approaching a few micrometers as in recent lab-on-a-chip systems (Craighead, 2000).

The main goal of this article is therefore to develop, summarize and discuss expressions for all regimes of operation relevant to flow-through microfluidic devices involving surface reaction. Particular emphasis is set on understanding transport in the fully developed region of the Graetz problem, an oft-encountered but seldomly studied regime in microfluidics. Through analysis and numerical simulations, we demonstrate that, for sufficiently thin channels, surface transport in microfluidic channels occur following moving front kinetics, similar to the transport in chromatographic columns. The models are illustrated with experimental

¹ In this contribution, the term boundary layer strictly applies to mass transfer boundary layers and never to momentum boundary layers. The latter are not present since the flows are fully developed laminar flows as a consequence of the small dimensions in microfluidic channels.

examples and kinetic data from the microfluidics literature. The overall analytic procedure provides criteria for designing and operating continuous microfluidic sensors based on convection, diffusion and reaction of multiple species, from cells to small molecules.

2. Physical model

2.1. Continuum transport model formulation

The general conservation equations, including a bulk reaction term, take the form:

$$\frac{\partial C_i}{\partial t} = -\vec{\nabla} \cdot \vec{N}_i + R_{vi}, \quad (1)$$

where the molar flux \vec{N} is

$$\vec{N} = -D_i \cdot \vec{\nabla} C_i + \vec{v} C_i. \quad (2)$$

Here, C_i is the volume concentration of the i th species, D_i is the diffusivity of the solute, \vec{v} is the fully developed velocity profile and R_{vi} is the volumetric rate of species creation in the bulk. For all surfaces, the boundary conditions on the molar flux \vec{N} represent the balance between flux to the surface and surface reaction.

$$\vec{u} \cdot \vec{N} = R_{si}. \quad (3)$$

\vec{u} is the surface unit vector (perpendicular and pointing inward). R_{si} is the inward flux of species i into the bulk, such that surface adsorption indicates a negative R_{si} term.

Solutions to these equations have been developed for various geometries, but only the case of flat plates will be considered here. The lithographic, embossing and ablation techniques (Madou, 2002) used to create most microfluidic systems produce broad and shallow channels. These channel shapes are desirable in most applications requiring readout of the surface-bound analyte. The fully developed three-dimensional (3D) laminar axial velocity profile $v(\text{height}, \text{width})$ can be represented as a simple function $v(\text{height})$ except close to the channel's side walls (Happel and Brenner, 1965). For studies of mass transfer in channels with cross-sections of different geometries, such as triangular channels produced from anisotropic etching of silicon (de Mas et al., 2003), or semi elliptical channels obtained through isotropic etching in glass (Fan and Harrison, 1994), solutions for simple cases have been provided in the literature for the fully developed region (Shah and London, 1978).

To further simplify the analysis, constant diffusivity is assumed for all species, even though the diffusivity in protein-dense biological media, such as cellular media, can be non-linear and highly dependent on protein size, shape and charge (Elowitz et al., 1999). Bimolecular surface reactions involving reversible binding of species are considered as being sufficiently general to encompass the majority of

surface association/dissociation reactions encountered in molecular biology. The rate equation takes the form

$$\frac{\partial C_s}{\partial t} = k_{\text{on}} C_w (C_{s0} - C_s) - k_{\text{off}} C_s, \quad (4)$$

where C_w is the analyte concentration (proteins, DNA oligomers, etc.) in the channel near the reactive wall. C_s , the concentration of surface bound analytes, is a function of position on the surface. C_{s0} is the total number of binding sites. k_{on} and k_{off} are respectively the association and dissociation rate constants of the bimolecular reaction (with units $\text{M}^{-1} \text{s}^{-1}$ and s^{-1}).

With the assumptions that the channel must be broad and shallow ($w \gg h$), and considering that bulk reaction is negligible compared to surface reactions ($R_{vi} = 0$), the transport equations and boundary conditions simplify to a 2D problem (Table 1). It is useful to scale the equations in order to reveal the dimensionless parameters governing the system. The resulting scaled equations take the form:

$$\frac{\partial \Theta(\eta, \zeta, \tau)}{\partial \tau} = \left(\frac{\partial^2 \Theta(\eta, \zeta, \tau)}{\partial \eta^2} + \frac{1}{Pe^2} \frac{\partial^2 \Theta(\eta, \zeta, \tau)}{\partial \zeta^2} \right) - v(\eta) \frac{\partial \Theta(\eta, \zeta, \tau)}{\partial \zeta}, \quad (5)$$

$$\frac{\partial \Theta_s(\zeta, \tau)}{\partial \tau} = \varepsilon Da [\Theta(\eta = 0, \zeta, \tau) (1 - \Theta_s(\zeta, \tau)) - \bar{K}_D \Theta_s(\zeta, \tau)], \quad (6)$$

with the dimensionless parameter groups for axial position $\zeta = zh^{-1} Pe^{-1}$, channel height $\eta = x/h$, normalized transverse diffusion time $\tau = Dt/h^2$, relative adsorption capacity $\varepsilon = C_0 h / C_{s0}$ and concentrations $\Theta_i = C_i / C_{i0}$. $Pe = Uh/D$ and $Da = k_{\text{on}} C_{s0} h / D$ are respectively the Péclet (Pe) and Damköhler number (Da). $\bar{K}_D = k_{\text{off}} / k_{\text{off}} (k_{\text{on}} C_0)$ is the dimensionless equilibrium dissociation constant and $v(\eta)$ is the normalized fully developed laminar flow velocity profile depending solely, in 2D, on the normalized height parameter η (Table 1). Eq. (5) and (6) are coupled by a flux balance at the wall (\vec{u} pointing inward)

$$\frac{\partial \Theta(\eta, \zeta, \tau)}{\partial \eta} \Big|_{\eta=[0,1]} = -\frac{1}{\varepsilon} \frac{\partial \Theta_s(\zeta, \tau)}{\partial \tau}. \quad (7)$$

2.2. Physical interpretation of ζ , Da and ε

The dimensionless parameters appearing in Eq. (5)–(7) simplify the equations and reveal important characteristics of the physical system. $\varepsilon = C_0 h / C_{s0}$ corresponds to the relative density of analytes between the bulk and the fully saturated surfaces (a measure of surface adsorption capacity relative to the bulk). It arises when matching the units of surface concentration and bulk concentration. A small ε indicates a high relative surface capacity leading to a longer saturation time. When $Da \gg 1$, the transport to the surface is strongly diffusion-limited, while at $Da \ll 1$, the transport becomes

Table 1

Complete equation system describing diffusion, convection, and reaction in a 2D channel in dimensional and scaled form

Coordinates	$x = [-h/2, h/2], z = [0, L]$ (O at center left of channel) $x = [0, h], z = [0, L]$ (O at lower wall left of channel)	
2D bulk transport	$\frac{\partial C(x,z,t)}{\partial t} = D \frac{\partial^2 C(x,z,t)}{\partial x^2} + D \frac{\partial^2 C(x,z,t)}{\partial z^2} - v(x) \frac{\partial C(x,z,t)}{\partial z}$	
Surface reaction	$\frac{\partial C_s(z,t)}{\partial t} = k_{\text{on}} C(x = x_{\text{wall}}, z, t) (C_{s0} - C_s(z, t)) - k_{\text{off}} C_s(z, t)$	
Normalized bulk transport	$\frac{\partial \Theta}{\partial \tau} = \frac{\partial^2 \Theta}{\partial \eta^2} + \frac{1}{Pe^2} \frac{\partial^2 \Theta}{\partial \zeta^2} - \frac{3}{2} (1 - 4\eta^2) \frac{\partial \Theta}{\partial \zeta}$ $\frac{\partial \Theta}{\partial \tau} = \frac{\partial^2 \Theta}{\partial \eta^2} + \frac{1}{Pe^2} \frac{\partial^2 \Theta}{\partial \zeta^2} - 6\eta(1 - \eta) \frac{\partial \Theta}{\partial \zeta}$	
Surface reaction	$\frac{\partial \Theta_s}{\partial \tau} = \varepsilon Da [\Theta_w(1 - \Theta_s) - \bar{K}_D \Theta_s]$	
	Both walls	One wall only
Boundary condition #1	$\left. \frac{\partial \Theta}{\partial \eta} \right _{\eta=0} = 0$ (symmetry)	$\left. \frac{\partial \Theta}{\partial \eta} \right _{\eta=0} = -\frac{1}{\varepsilon} \frac{\partial \Theta_s}{\partial \tau}$ (reaction at wall 1)
Boundary condition #2	$\left. \frac{\partial \Theta}{\partial \eta} \right _{\eta=1/2} = -\frac{1}{\varepsilon} \frac{\partial \Theta_s}{\partial \tau}$ (reaction at walls)	$\left. \frac{\partial \Theta}{\partial \eta} \right _{\eta=1} = 0$ (insulation at wall 2)
Initial, inlet, and outlet conditions	$\Theta(\eta, \zeta, \tau = 0) = 0, \Theta_s(\zeta, \tau = 0) = 0, \Theta(\eta, \zeta = 0, \tau) = 1, \left. \frac{\partial \Theta}{\partial \zeta} \right _{\zeta=\infty} = 0$	

limited by the reaction at the surface and a flat (constant) concentration profile can be expected across the channel.

The diffusion/convection length scale, ζ , also known as the Graetz number (Gr), is an important parameter in this study as it controls the transitions in mass transfer from the entrance region to the fully developed region. Physically, at $\zeta = 1$, the time scale required for diffusion across the channel height becomes the same as the time scale required for crossing a distance z at velocity U . For $\zeta < 1$, the convection time scale is shorter than the diffusion time scale and a portion of the analytes in the channel are not able to “reach” the reactive surface exiting the sensing region. The result is the appearance of a mass transfer boundary layer. For $\zeta > 1$, analytes have plenty of time to diffuse to the reactive surfaces and no mass transfer boundary layer develops. In the case of a reaction on both top and bottom walls, the diffusion time scale becomes $\bar{t}_d = h^2/4D$ as a molecule is at most half a channel height away from a reactive wall. Nevertheless, for consistency, the scaling of τ and ζ based on reactive surface will be used throughout this paper.

Table 2 provides typical operating conditions and corresponding dimensionless parameters for three often studied microfluidic applications: antibody–antigen (Ab–Ag) interaction, Streptavidin–Biotin affinity, and DNA hybridization. These examples span the range of applications, typical density of immobilized probes or “reactive sites”, and lengths scales (μm to mm).

3. Analytic solutions and numerical simulations

The non-linear convection/diffusion/reaction problem summarized in Table 1 can be solved numerically (e.g., by using finite element methods) to provide an accurate solution to a specified set of parameters. Analytic solutions, when feasible, provide insight into the relationship between parameters (space, time, rate constants, etc.) and dependent variables (bulk and surface concentration, capture fraction, etc.). No complete analytic solutions exist to the whole

problem due to the non-linear surface reaction term, but the solution space can be segmented into physically relevant parameter regimes for which analytic solutions exist. In particular, the transport equations can be decomposed in two accurate analytic solutions for $\zeta \gg \zeta_{\text{crit}}$ and $\zeta \ll \zeta_{\text{crit}}$, where ζ_{crit} represents the critical value from which the two analytic models have the same relative error compared to the numerical solution. These solutions can be subdivided once more depending on whether the surface Damköhler number is finite (partially reaction-limited) or infinite (fully diffusion-limited). The numerical simulations and analytic solutions provide complementary physical insights into coupled transport and reaction phenomena in microfluidic applications while also serving as a firm basis for device design.

The complete transport problem with a bimolecular reaction at one or both surfaces (Table 1) was simulated by finite element methods implemented in FEMLAB (Comsol AB, Stockholm, Sweden). Since many studies have been conducted for the entrance case $-\zeta \ll 1$, which is particularly relevant to SPR (Glaser, 1993; Goldstein et al., 1999; Yarmush et al., 1996), the present simulations are primarily aimed to characterize the fully developed region.

3.1. The Graetz problem in mass transfer

In most applications involving high relative adsorption capacity (low ε), the bulk concentration reaches a steady state value much before the surface has been significantly saturated. The transport in the bulk can then be assumed to be in pseudo steady state with respect to the surface at all times. Moreover, in most microfluidic applications, the axial convection is much faster than the axial diffusion, i.e., $Pe \gg 1$. Pe is usually on the order of 10^2 – 10^4 . As a result axial diffusion can be neglected and the simplified, scaled, transport problem, known as the Graetz problem in heat transfer, then takes the form:

$$\frac{\partial^2 \Theta(\eta, \zeta)}{\partial \eta^2} = v(\eta) \frac{\partial \Theta(\eta, \zeta)}{\partial \zeta}. \quad (8)$$

Table 2
Three typical examples of microfluidic applications

	Protein A33 immunoassay	Streptavidin/bBSA binding in suspended microresonator	Single mutation detection using DNA- oligomer hybridization
Flow rate Q	$1 \mu\ell \text{ min}^{-1}$	$0.0024 \mu\ell \text{ min}^{-1}$	$1 \mu\ell \text{ min}^{-1}$
Width w	0.5 mm	0.02 mm	0.5 mm
Height h	0.05 mm	0.001 mm	0.05 mm
Average velocity U	0.67 mm s^{-1}	2 mm s^{-1}	0.67 mm s^{-1}
Diffusivity D	$\sim 10^{-4} \text{ mm}^2 \text{ s}$	$6 \times 10^{-5} \text{ mm}^2 \text{ s}$	$4.3 \times 10^{-5} \text{ mm}^2 \text{ s}$
Length of bed L	0.1 mm	2 mm	400 μm (round spot)
$\zeta_L = \frac{LDw}{Qh}$	0.007	60	0.01
k_{on}	$2.4 \times 10^5 \text{ M}^{-1} \text{ s}^{-1}$	$1.2 \times 10^5 \text{ M}^{-1} \text{ s}^{-1}$ ^a	$\sim 1.2 \times 10^5 \text{ M}^{-1} \text{ s}^{-1}$ ^b
k_{off}	$3.5 \times 10^{-3} \text{ s}^{-1}$	~ 0	$\sim 2.1 \times 10^{-4} \text{ s}^{-1}$ ^b
C_{s0}	70 fmol mm^{-2}	70 fmol mm^{-2} ^a	8 fmol mm^{-2}
C_0	$0.1 \mu\text{M}$ ^c	$0.1 \mu\text{M}$ ^c	$0.1 \mu\text{M}$ ^c
$\varepsilon = C_0 h / C_{s0}$	0.07	0.0014	0.6
$Da \equiv k_{\text{on}} C_{s0} h / D$	~ 10	0.14	~ 1
$Pe = Uh/D$	335	17	335
$\bar{K}_D = k_{\text{off}} / k_{\text{on}} C_0$	0.14	~ 0	0.02
Reference	Catimel et al. (1997)	Burg (2004)	Wang et al. (2003)

^aPolzius et al. (1997).

^bOkahata et al. (1998).

^cOrder of magnitude commonly found in cell signaling proteins.

The coupled, nonlinear boundary condition found in Eq. (6), implies that the system composed of Eq. (7) and (8) generally has to be solved numerically. However, in cases where $C_s \ll C_{s0}$ (at sufficiently small times), the bimolecular surface reaction, Eq. (4), reduces to a pseudo first order reaction and the boundary condition becomes linear:

$$\left. \frac{\partial \Theta(\eta, \zeta, \tau)}{\partial \eta} \right|_{\eta=0} = Da \Theta(\eta = 0, \zeta, \tau). \quad (9)$$

The linear system, which is relevant to practical cases, can be solved analytically (Table 3) using the method of separation of variables to obtain an eigenfunction expansion of the solution (Papoutsakis and Ramkrishna, 1981). The exact form of the eigenfunction expansion has been provided for the circular pipe and parallel plate geometry with rapid reaction at both walls (Brown, 1960). In Table 3, we also introduce the exact form of the eigenfunction expansion for the case of parallel plates with reaction at only one wall, including the first five expansion coefficients and eigenvalues for the fully diffusion-limited case.

These analytic solutions converge slowly: after a five term expansion, the maximum relative error on the concentration is still $\sim 5\%$. However, the complete set of functions is only necessary when the full 2D concentration profile must be mapped. For most practical applications, the time scale of saturation of the substrate or the fraction of mass bound to the surface is of primary interest rather than the detailed concentration profile in the fluid channel. In those cases, the general solution can be separated according to different

parameter regimes and analytic solutions calculated with respect to the velocity-weighted, or “mixed-cup” bulk concentration

$$\Theta_b(\zeta, \tau) = \int_{\text{cross section}} \Theta(\eta, \zeta, \tau) v(\eta) d\eta, \quad (10)$$

where $v(\eta)$ is the normalized velocity profile (see Table 3).

3.2. Capture fraction of a bed and saturation time scales

The total capture fraction of a bed of length L represents the fraction of analytes adsorbed on the surface after one passage, specifically:

$$f(L) = \frac{C_0 - C(L)}{C_0} = 1 - \Theta_b(L). \quad (11)$$

The saturation time scale is defined herein as the time required for saturating 95% of the available binding sites for the analyte. When the reaction is fully diffusion-limited, solutions depend only on the diffusivity, and for reaction limited situations, only the reaction constant is involved. For intermediate cases, the saturation time will depend on both diffusion and reaction rates, making it possible to express it as a function of Da . This parameter and the diffusion/convection length scale ζ , are the two main parameters for characterizing surface capture and transport phenomena in microfluidic devices. The possible regimes are summarized in Table 4 and discussed in detail in the following sections.

Table 3
The scaled Graetz problem for a first order reaction on both walls (symmetric case) and one wall (asymmetric case)

	Symmetric case	Asymmetric case
Coordinates	$\eta = [-1/2, 1/2], \zeta = [0, L/hPe]$ (O at center left of channel)	$\eta = [0, 1], \zeta = [0, L/hPe]$ (O at lower wall left of channel)
Bulk transport Graetz problem	$\frac{\partial^2 \theta}{\partial \eta^2} = \frac{3}{2}(1 - 4\eta^2) \frac{\partial \theta}{\partial \zeta}$	$\frac{\partial^2 \theta}{\partial \eta^2} = 6\eta(1 - \eta) \frac{\partial \theta}{\partial \zeta}$
Boundary condition #1	$\frac{\partial \theta}{\partial \eta} \Big _{\eta=0} = 0$ (symmetry)	$\frac{\partial \theta}{\partial \eta} \Big _{\eta=0} = -\frac{1}{\varepsilon} \frac{\partial \theta_s}{\partial \tau}$ (reaction at wall 1)
Boundary condition #2	$\frac{\partial \theta}{\partial \eta} \Big _{\eta=1/2} = -\frac{1}{\varepsilon} \frac{\partial \theta_s}{\partial \tau}$ (reaction at walls)	$\frac{\partial \theta}{\partial \eta} \Big _{\eta=1} = 0$ (insulation at wall 2)
Surface reaction	$\frac{\partial \theta_s}{\partial \tau} \approx \varepsilon Da \theta_w$, valid for $\theta_s(\zeta, \tau) \ll 1$ (unsaturated surface, pseudo first order)	
Axial boundary conditions	$\Theta(\eta, \zeta = 0) = 1$	
General form of solution	$\Theta(\eta, \zeta) = \sum_{i=1}^{\infty} a_i G_i(\lambda_i, \eta) \exp(-\frac{\lambda_i^2 \zeta}{6})$	
Basis function $G_i(\lambda_i, \eta) =$	$\exp(-\lambda_i \eta^2 / 2) M(\frac{1}{4} - \frac{\lambda_i}{16}, \frac{1}{2}, \lambda_i \eta^2)^a$	$\frac{1}{2} \exp(\frac{\lambda_i \eta(1-\eta)}{2}) \{ \bar{M}(\frac{1}{4} - \frac{\lambda_i}{16}, \frac{1}{2}, \lambda_i(1/2 - \eta)^2) - Cst(\lambda_i)(1 - 2\eta) \bar{M}(\frac{3}{4} - \frac{\lambda_i}{16}, \frac{3}{2}, \lambda_i(1/2 - \eta)^2) \}^b$
Velocity-averaged solution	$\Theta_b(\zeta) = \sum_{i=1}^{\infty} A_i \exp(-\frac{\lambda_i^2 \zeta}{6})$, where $A_i = \int_{\eta=0}^1 a_i G_i(\lambda_i, \eta) v(\eta) d\eta$	

^a $M(a, b, \zeta) = \sum_{k=0}^{\infty} \frac{(a)_k}{(b)_k} \frac{\zeta^k}{k!}$ is the confluent hypergeometric function, or Kummer M function (Abramowitz and Stegun, 1970).

^b $\bar{M}(a, b, \lambda_i(1/2 - \eta)^2) = \frac{M(a, b, \lambda_i(1/2 - \eta)^2)}{M(a, b, 1/4 \lambda_i)}$ is the Kummer M function normalized to 1 at $\eta = 0$ and 1. The constant for the asymmetric basis functions reads: $Cst(\lambda) = \frac{(\lambda - 4)M(\frac{1}{4} - \frac{\lambda}{16}, \frac{1}{2}, \frac{\lambda}{4}) + (\lambda + 4)M(-\frac{3}{4} - \frac{\lambda}{16}, \frac{1}{2}, \frac{\lambda}{4})}{(\lambda - 12)M(\frac{7}{4} - \frac{\lambda}{16}, \frac{3}{2}, \frac{\lambda}{4}) + (\lambda + 4)M(\frac{3}{4} - \frac{\lambda}{16}, \frac{3}{2}, \frac{\lambda}{4})} \times \frac{M(\frac{3}{4} - \frac{\lambda}{16}, \frac{3}{2}, \frac{\lambda}{4})}{M(\frac{1}{4} - \frac{\lambda}{16}, \frac{1}{2}, \frac{\lambda}{4})}$.

Table 4
Result summary

Regime	Characteristics	Capture fraction	Surface concentration	Surface saturation time	Applications (microfluidics)	Method reference
Entrance region $\zeta < \zeta_{crit}$ $n_w = 1$ (asym. reaction)	$Da = \infty$ Fully analytical solutions	$f(\zeta, t) = 1 - \Theta_b(\zeta, t)$ $1 - \exp\left(-\frac{3n_w}{\Gamma(1/3)}(3\zeta/2)^{2/3}\right)$	$\Theta_s(\zeta, t)$ or effective rate constant $\frac{\partial(\Theta_s)}{\partial t} = k_{on}^{eff} C_0(1 - (\Theta_s)) - k_{off}^{eff}(\Theta_s)$	constant $\Theta_s(\zeta, T_{0.95}) = 0.95\Theta_{s-eq}$ $T_{0.95}(\zeta, \bar{t}_d, \bar{K}_D, \epsilon);$	Surface plasmon resonance (SPR), high flow rates in thick channels,	Deen (1998), Lok (1983)
$n_w = 2$ (sym. reaction)	$Da = finite$ Numerical solutions	$1 - \Theta_b(\zeta, t)$ Numerical solutions	$k_{on}^{eff} = \frac{k_{on}}{1 + 0.95Da(1 - (\Theta_s))\zeta_L^{1/3}}$ $k_{off}^{eff} = \frac{k_{off}}{1 + 0.95Da(1 - (\Theta_s))\zeta_L^{1/3}}$	Numerical solutions	SPR, on chip DNA hybridization, Ab-Ag complexes	Mason (1999)
Fully developed region $\zeta < \zeta_{crit}$	Daarbitrary, unsaturated surface $\Theta_s \ll 1$	$f(t) = 1 - \exp\{-n_w \bar{k}_d/r(Da)\zeta\}$ (valid for pseudo first order reactions) (See Fig. 3 for \bar{k}_d/r)	$\Theta_s \approx \frac{\bar{k}_d/r \cdot \epsilon t}{Da(1 - \Theta_s)\zeta^{1/3}} \gg 1$ with $\Theta_b(\zeta) = \exp\{-n_w \bar{k}_d/r \cdot \zeta\}$	Numerical solutions	Heat/mass transfer in long, narrow channels (nonspecific adsorption control)	Shah and London (1978)
$Da \gg 1$ (Wave regime)	$f(t) = 1 - \Theta_b(\zeta_L + \bar{\zeta}_{shift})$	$\bar{\zeta}_L = \frac{L}{Peh} - \frac{U_{eff}t}{U\bar{t}_d}, \bar{\zeta}_{shift} = \frac{1}{\epsilon(1 + \bar{K}_D)}$	$\Theta_s(\bar{\zeta}) \approx \frac{\Theta_b(\bar{\zeta})}{1 + \bar{K}_D}$	$T_{1,00} \approx L/U_{eff}$ where $U_{eff} = \frac{\epsilon + n_w(1 + \bar{K}_D)^{-1}}{\epsilon U}$	Mass transfer in long, narrow channels: Non specific adsorption, single cell analysis, passivation, arbitrary wall resistance, fine structures	Rhee and Amundson (1989)
$Da \ll 1$ (Wave regime)	$f(t) = 1 - \Theta_b(\bar{\zeta}_L)$	$\sigma = \sqrt{\frac{2}{\pi}} \frac{1}{n_w \bar{k}_d/r(Da\epsilon t)}$	$\Theta_s(\bar{\zeta}) \approx \frac{\Theta_b(\bar{\zeta})}{1 + \bar{K}_D}$	with wave regime valid for $L \gg \frac{U\bar{t}_d}{n_w \bar{k}_d/r}$	High concentration of analytes (non conventional geometries, Complex kinetics, non linear diffusion)	Cazes and Scott (2002) This paper
Full solutions : ζ arbitrary	Varies	Mostly numerical solutions				Varies

Decomposition of the Graetz problem, with bimolecular surface reaction, in its various asymptotic solutions. Parameters of interest are the fraction of the total number of analytes captured by the surface $f(\zeta)$ and the time required to saturate the surface in various regimes. In intermediate cases, where an analytic solution is not possible, an upper bound is given and reference to further analysis is provided.

3.3. Solutions for fully diffusion-limited situations

3.3.1. Entrance region ($\zeta \ll 1$) and $Da \rightarrow \infty$

The mass transfer entrance region arises when the diffusion time scale ($\bar{t}_d = h^2/D$) is much greater than the axial convection time scale ($\bar{t}_c = z/U$), such that $\zeta = \bar{t}_c/\bar{t}_d \ll 1$ and a mass transfer boundary layer of thickness $\delta \ll h$ appears. This problem was analyzed early in the SPR literature (Lok et al., 1983). It is also common in flow-through devices, such as quartz microbalances and any other surface-based sensors.

The bulk concentration along the channel length can be computed using a mass transfer coefficient approach (Bird et al., 2002)

$$\frac{\partial \Theta_b(\zeta, \tau)}{\partial \zeta} = -n_w Sh (\Theta_b(\zeta, \tau) - \Theta_w(\zeta, \tau)), \quad (12)$$

where the Sherwood number Sh , is the mass transfer coefficient (k_m) scaled by the characteristic length scale (l) and the diffusion coefficient (D) (i.e., $Sh \equiv k_m l/D$). The Sherwood number, is defined as the ratio of the gradient at the wall divided by the driving force for mass transport:

$$Sh \equiv \frac{(\partial \Theta(\eta, \zeta)/\partial \eta)_{\text{wall}}}{\Theta(\eta, \zeta)_{\text{bulk}} - \Theta(\eta, \zeta)_{\text{wall}}}. \quad (13)$$

The Sherwood number is expressed on a per wall basis. The index n_w takes into account the number of walls participating in the reaction, $n_w = 1$ for the asymmetric reaction case and $n_w = 2$ for the symmetric case.

Assuming the surface concentration is 0 ($Da \rightarrow \infty$) the Sherwood number of the entrance (E) region yields the well-known result:

$$Sh_E = \frac{3}{\Gamma(1/3)} \left(\frac{3\zeta}{2} \right)^{-1/3} = 0.978 \zeta^{-1/3}. \quad (14)$$

The dependence on $\zeta^{-1/3}$ indicates that, as $\zeta \rightarrow 0$, mass transfer to the surface will become very large and the system will become reaction-limited. Consequently, this regime of operation is preferred for the determination of reaction rate constant (as in SPR systems).

By solving Eq. (12) with the expression of the Sherwood number found in Eq. (14), and using the axial boundary condition, $\Theta_b(\zeta = 0) = 1$, the bulk concentration remaining after a distance ζ can be expressed as

$$\begin{aligned} \Theta_{bE}(\zeta) &= \exp \left\{ -\frac{3n_w}{\Gamma(1/3)} \left(\frac{3\zeta}{2} \right)^{2/3} \right\} \\ &= \exp \{-1.467 n_w \zeta^{2/3}\}. \end{aligned} \quad (15)$$

For sufficiently large Da , the flux to the surface is mass transfer-limited and constant at any given position down the channel. As a result, the surface concentration increases

linearly in time and the saturation time can be expressed as

$$\begin{aligned} \frac{n_w}{\varepsilon} \frac{\partial \Theta_s}{\partial \tau} + \frac{\partial \Theta_b}{\partial \zeta} \Big|_{z=L} &= 0 \\ \Rightarrow \Theta_s &= \frac{\varepsilon}{n_w} Sh_E(L) \Theta_b(L) \tau. \end{aligned} \quad (16)$$

For small ζ , $\Theta_b(\zeta) \rightarrow 1$. The time scale for which the surface becomes 95% saturated, i.e., $\Theta_{s\text{-sat}} \rightarrow 0.95(1 + \bar{K}_D)^{-1}$, is thus given by

$$\begin{aligned} T_{0.95} &= \frac{h^2}{\varepsilon D(1 + \bar{K}_D) \Theta_b(L)} \frac{0.95}{0.978} \zeta^{1/3} \\ &\approx 0.97 \frac{h^2}{\varepsilon D(1 + \bar{K}_D)} \zeta^{1/3}. \end{aligned} \quad (17)$$

This expression is valid when the transport is strongly diffusion limited. This situation arises in the case of slow diffusing species such as DNA strands or large proteins flowed over a bed of highly concentrated probes.

3.3.2. Fully developed region ($\zeta \gg 1$), $Da \rightarrow \infty$

For the fully developed region, diffusivity is fast enough compared to the convective time scale so that no boundary layer appears. The linearization of the flow profile made in Section 3.3.1 no longer holds since the whole channel now participates in the reaction, and the full solution to the transport equations found in Table 1 must be considered.

For the fully developed region, the mass transfer coefficient can be calculated using the definition of the Sherwood number in Eq. (13). By integrating Eq. (8), a relation between the bulk concentration and the flux at the wall is found to be

$$\frac{\partial \Theta_b(\zeta)}{\partial \zeta} = -n_w \left(\frac{\partial \Theta(\eta, \zeta)}{\partial \eta} \right)_{\text{walls}}. \quad (18)$$

Using these relations and applying them to the eigenfunction expansion (Table 3), the analytic expression for the Sherwood number for large ζ ($Da \rightarrow \infty$) is given by (Shah and London, 1978)

$$Sh_{FD} = \frac{\lambda_1^2}{n_w 6} = \begin{cases} 2.4304 & \text{asymmetric reaction case,} \\ 3.7704 & \text{symmetric reaction case.} \end{cases} \quad (19)$$

The first eigenvalue λ_1 of the solution expansion is different whether symmetric or asymmetric reaction is assumed.

Substituting the fully developed Sherwood number in the general mass transfer equation, Eq. 12, the expression of the bulk concentration as a function of distance becomes

$$\Theta_{bFD}(\zeta) = \exp(-n_w Sh_{FD}) = \exp \left(-\frac{\lambda_1^2 \zeta}{6} \right). \quad (20)$$

3.4. Critical ζ value and mass transfer regime change

The successful design and characterization of a sensor will necessarily require the use of the proper transport model

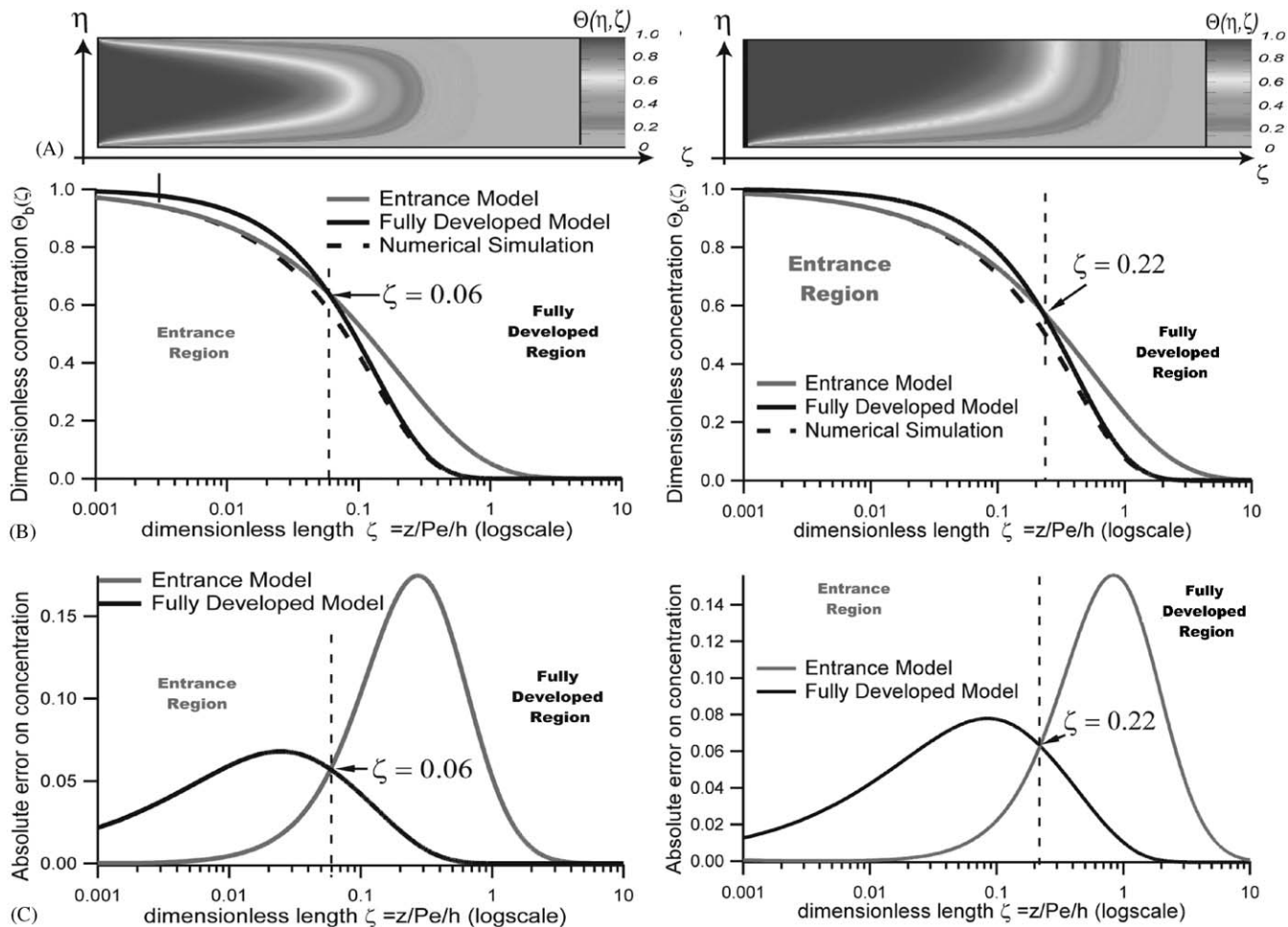


Fig. 2. Numerical simulation of the Graetz problem for parallel plate geometry and diffusion limited reaction at both walls. Left: symmetric reaction, Right: Asymmetric reaction. (A) Numerical simulation of the concentration profile in dimensionless units ($\eta = x/h$, $\zeta = z/Pe/h$). The ζ axis is presented in logarithmic scale to emphasize the boundary layer at $\zeta \ll 1$. (B) Plot of the normalized bulk concentration $\Theta_b(\zeta)$. Comparison of the asymptotic models for small ζ (gray, entrance region, see Eq. (15) and large ζ (black, fully developed region, see Eq. (20) with the numerical model (black dotted line) over 4 log units in ζ . (C) Absolute error on the bulk concentration $\Theta_b(\zeta)_{\text{analytic}} - \Theta_b(\zeta)_{\text{numerical}}$.

for a particular device. The absolute maximum error committed by selecting the wrong model between Eqs. (15) and (20) goes as high as 18% while the relative error (“model value”/“numerical value”) is unbounded (Fig. 2).

The simulation presented in Fig. 2 establishes the domain of validity of the two asymptotic models in the fully convective ($Pe \rightarrow \infty$) and diffusion-limited ($Da \rightarrow \infty$) regime at steady state (Graetz Problem, Eq. (8)). The absolute error on $\Theta_b(\zeta)$ on both models is plotted as a function of ζ (Fig. 2) for the case of reaction at one or both walls. The point at which the error is the same for both models is identified as the transition point (ζ_{crit}) between the entrance region and the fully developed region. Its value was found to be $\zeta_{\text{crit}} = 0.06$ and $\zeta_{\text{crit}} = 0.22$ for the symmetric and asymmetric reaction cases respectively. These values are consistent since, as mentioned earlier, the real height scale in the case of the symmetric reaction is $h/2$, which explains why ζ_{crit} is smaller by a factor of ~ 4 in the symmetric case.

3.5. Solutions for partially diffusion-limited situations

3.5.1. Entrance region: bimolecular reaction or finite Da numbers

Typically in biology, binding reactions are not sufficiently fast to be assumed purely mass transfer-limited. Bimolecular surface Damköhler numbers range from less than 1 for very thin structures and slow binding species, such as DNA, to more than 10 for faster surface reactions, such as protein–protein interactions. In general, the higher the probe density at the surface (C_{s0}), the faster the effective reaction will be and the higher the Damköhler number.

For first order reactions with finite Damköhler numbers or bimolecular reaction kinetics, a similarity solution is no longer possible and only a partially analytic solution can be found (Hsu, 1968). Nevertheless, this regime, which is a generalization of the one described in Section 3.3.1, is useful under a much larger set of reaction conditions often

appearing in SPR analysis or any sensor operating in the entrance regime.

In the past, several two-compartment numerical models have been designed to compute the effective saturation time scales for this type of problem (Myszka et al., 1998; Vijayendran and Leckband, 2001). Using a semi analytical approach, others have obtained similar results (Mason et al., 1999; Wofsy and Goldstein, 2002). They defined the effective reaction rate equation to be

$$\frac{\partial \langle \Theta_s \rangle}{\partial t} = k_{\text{on}}^{\text{eff}} (1 - \langle \Theta_s \rangle) - k_{\text{off}}^{\text{eff}} \langle \Theta_s \rangle. \quad (21)$$

$\langle \Theta_s \rangle$ is the average concentration along the reaction zone of length L . The effective association and dissociation first order rate constants are found in Table 4. A high Sherwood number, indicating fast mass transport, brings these equations back to the simple bimolecular rate equation found in Eq. (4). Analytic expressions for the capture fraction and saturation time only exist for the cases of fully diffusion-limited reaction at the surface. In this case, due to the dependence in Θ_s of the effective reaction rates, the rate equation has to be solved numerically.

3.5.2. Fully developed region: bimolecular reaction or finite Da

For transport outside the boundary layer regime, the solution derived here is much more tractable than the one presented in Section 3.5.1. Furthermore, as Da decreases, the error on the numerical model provided by the fully developed asymptotic model decreases, thus making it much more useful than the boundary layer model under certain conditions. The derivation of the results is analogous to the ones in Sections 3.3.2 and 3.5.1. The Robin boundary condition, Eq. (9), is used to link the flux at the wall to the concentration near the wall $\Theta_w(\eta, \zeta)$ in Eq. (18). Using these relations, the expression of the effective Sherwood number for an arbitrary first order reaction becomes

$$Sh_{FD}(Da) \equiv \frac{1}{\frac{1}{\bar{k}_{d/r}} + \frac{1}{\bar{k}_s}} \rightarrow \left(\frac{1}{\frac{\lambda_1^2(Da)}{6n_w}} + \frac{1}{Da} \right)^{-1}, \quad (22)$$

This result is analogous to the mass transfer coefficient approach used in the boundary layer theory (Bird et al., 2002). The two terms represent mass transfer rates $\bar{k}_{d/r}$ (bulk) and \bar{k}_s (surface) added in series such that, when $Da \rightarrow \infty$, $Sh_{FD}(\infty) \rightarrow \lambda_1^2/6n_w$ and when $Da \rightarrow 0$, $Sh_{FD}(0) \rightarrow 0$. In this case, however, the partially reaction limited bulk transfer coefficient $\bar{k}_{d/r}$ depends not only on the flow and diffusion properties in the bulk, but also on the reaction rate at the surface. The diffusion/reaction mass transfer coefficient (per surface) $\bar{k}_{d/r}$ as we define it here,

$$\bar{k}_{d/r}(Da) = \frac{\lambda_1^2(Da)}{n_w 6}, \quad (23)$$

is therefore a function of Da .

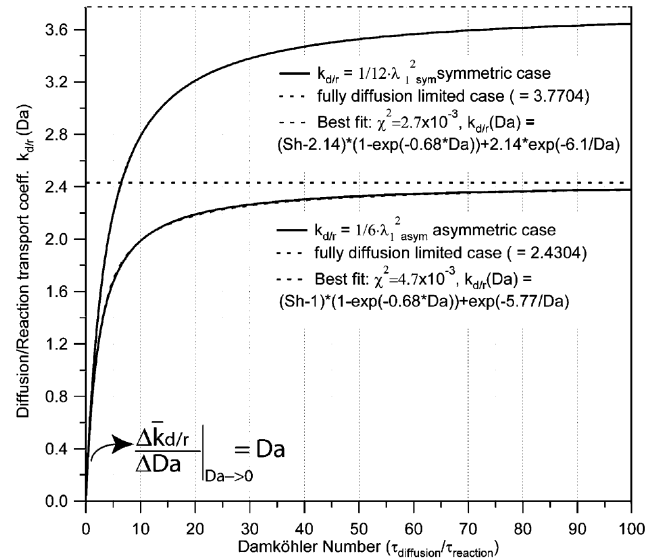


Fig. 3. Plot of the effective diffusion/reaction transport coefficient $\bar{k}_{d/r}$ of the Graetz problem as a function of the Da number (i.e. including finite first order reaction rate) for the asymmetric case (lower) and the symmetric case (upper). The dotted horizontal lines mark the respective maxima, equivalent to the Sherwood number $Sh_{\text{sym}} = 3.7704$, $Sh_{\text{asym}} = 2.4304$. The dotted curves represent the best fit according to a three-parameter model: $\bar{k}_{d/r}(Da) \approx (\bar{k}_{d/r}(Da \rightarrow \infty) - \gamma) \exp(-\kappa_1 Da) + \gamma \exp(-\kappa_2/Da)$ and the χ^2 error estimation is given. From the numerical calculations, we also observe that, when $Da \rightarrow 0$, $\bar{k}_{d/r}(Da) \approx Da$ and the relation becomes even simpler to use.

Replacing the value of Sh with $Sh_{FD}(Da)$ in Eq. (12) and the value of Θ_w by its flux value using Eq. (9), then Eq. (18), an alternative notation for the transport coefficient involving both diffusion and reaction is found to be

$$\begin{aligned} \frac{\partial \Theta_b(\zeta)}{\partial \zeta} &= -n_w Sh_{FD}(Da) (\Theta_b(\zeta) - \Theta_w) \\ &= -n_w \bar{k}_{d/r}(Da) \Theta_b(\zeta). \end{aligned} \quad (24)$$

The value of $\bar{k}_{d/r}(Da)$ is plotted in Fig. 3.

Using an identical approach as in Section 3.3.2, the generalized bulk concentration profile along the axis for an arbitrary first order reaction is

$$\Theta_{bFD}(\zeta) = \exp(-n_w \bar{k}_{d/r} \zeta) = \exp\left(-\frac{\lambda_1^2(Da)}{6} \zeta\right). \quad (25)$$

This time, the first eigenvalue λ_1 will vary with respect to Da and will have to be determined numerically, using the basis function described in Table 3 and applying the second boundary condition, found in Eq. (9). The eigenvalue equation which provided the numerical values of $\lambda_1^2/6n_w$ vs Da in Fig. 3 is intractable analytically due to its algebraic complexity. To allow a quick approximate calculation of $\bar{k}_{d/r}$, we therefore provide an approximation of its numerical solution by a three parameter fit (see Fig. 3).

Eq. (27) will only be valid when the surface is not saturated, such that the pseudo first order reaction approximation

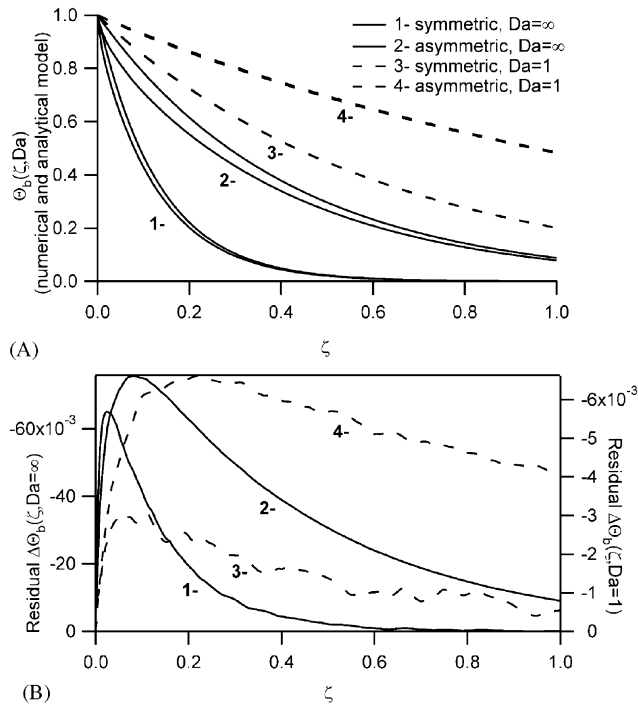


Fig. 4. Numerical simulation of surface transport with a first order surface reaction for parallel plate geometry in the fully developed region. (A) Plot of the normalized bulk concentration $\Theta_b(\zeta)$ for the fully diffusion-limited case ($Da = \infty$) and for a partially reaction-limited case ($Da = 1$). Comparison of the asymptotic models with the numerical models (lowest in the pair of lines for $Da = \infty$, difference undistinguishable for $Da = 1$) for both symmetric and asymmetric reaction cases in the fully developed region. (B) Absolute error on the bulk concentration $\Delta\Theta_b(\zeta) = \Theta_b(\zeta)_{\text{numerical}} - \Theta_b(\zeta)_{\text{asymptotic-FD}}$. The error for the case where $Da = 1$ (dashed lines), is one order of magnitude lower than for $Da = \infty$, which explains why the asymptotic and numerical models coincide in A.

can be used. For very long capture beds, it implies that the saturation time constant of the bed can no longer be evaluated by assuming a pseudo steady state profile above the bed. A moving front, or wave-like approach has to be used and the saturation time has to be deduced from the velocity of the resulting wave front (see below).

3.6. Critical ζ value and regime change for finite Da

The critical value of ζ at which the boundary layer model is no longer better than the fully developed model cannot be determined using a straight forward approach in the case of finite Damköhler numbers since no analytic solution exists for the entrance region case. The limit needs to be computed numerically for every value of Da , which renders the process tedious. However, it is important to note that the usefulness of the fully developed model over the entrance region model increases as Da decreases. This can be justified by showing that the error on the model decreases as Da decreases. This behavior is presented graphically in Fig. 4. The algebraic details of the proof are presented in Appendix A.1. By

keeping only the first term in the expansion, the error on $\bar{k}_{d/r}(Da)$ is 4–6 times less when $Da \rightarrow 1$. The repercussion on Θ_b is to reduce the error caused by using the fully developed region model over for the entrance region by one order of magnitude (Fig. 4B).

4. Wave-like propagation of bulk concentration

4.1. Convection-limited transport

Reactions in long and thin structures naturally yield higher ζ and lower Da compared to the usually thicker microfluidic channels. The suspended microresonator device introduced by Burg et al., has this characteristic (see Table 2, entry 2). Physically, these numbers ($\zeta = 60$, $\varepsilon = 10^{-3}$, $Da = 0.1$) indicate a rapid axial depletion of the bulk and a diffusion time scale smaller than the reaction time scale. At low enough flow rates, the residence time in the device will also be much longer than the time required for the analyte to bind at the surface, such that we also enter in a convection-limited regime. This behavior can be characterized by a convection/reaction number,

$$\zeta_L Da = \frac{DL}{Uh^2} \frac{k_{on} C_{s0} h}{D} = \frac{k_{on} C_{s0} L}{Uh}, \quad (26)$$

which compares the time scale for an analyte molecule to either react at the surface or exit the surface reaction area by convection, assuming fast axial diffusion. In certain notations, this convection/reaction number is known as Damköhler's first number (the diffusion/reaction Damköhler number (Da) used throughout this paper being the second one). When $\zeta_L Da \ll 1$, the transport is reaction limited, while it becomes convection-limited for $\zeta_L Da \gg 1$. In the latter case, binding occurs near the entrance, totally depleting the bulk. As the surface saturates, more sample will move further down the channel to bind and saturate the walls. The result is a bulk concentration front propagating in a wave-like fashion throughout the channel. This behavior can be derived from the transport equations (Table 1) and characterized using a kinematic wave—or shock solution—approach (Rhee et al., 1989).

4.2. Determination of the propagation velocity

When an analyte solution flows over a high capacity surface ($\varepsilon \ll 1$), the solution profile in the bulk of the channel reaches a quasi steady-state above the reaction surface. After a time on the order of the reaction time scale has elapsed, the surface starts to saturate and a pattern is created which propagates into the channel at a constant velocity smaller than the fluid velocity U . This behavior can be simply modeled for limiting cases very far behind and ahead of the moving front. It can be interpolated for cases in between. The analytical approach to this task is analogous to capture in a packed bed in liquid chromatography, since both cases

exhibit high surface to volume ratio. The elution time for the solution can therefore be calculated using a similar approach and depends on the relative adsorption capacity ε and the tightness of binding \bar{K}_D .

A simple model of the adsorption can be derived from a mass balance between the bound mass and the bulk mass along the channel. By integrating the normalized transport equation found in Eq. (5) across the channel height and using the normalized boundary condition in Eq. (7), the bulk transport equation becomes

$$\frac{\partial \Theta_b(\zeta)}{\partial \zeta} + \frac{\partial \bar{\Theta}(\zeta, \tau)}{\partial \tau} + \frac{n_w}{\varepsilon} \frac{\partial \Theta_s(\zeta, \tau)}{\partial \tau} = 0, \quad (27)$$

where $\bar{\Theta}(\zeta, \tau)$ is the cross-section-averaged concentration and $\Theta_b(\zeta, \tau)$ is given in Eq. (10). Applying a dimensionless variable change of the form

$$\bar{\zeta} = \zeta - \frac{U_{\text{eff}}}{U} \tau, \quad (28)$$

the problem can be expressed in the referential of the moving concentration front

$$U \frac{\partial \Theta_b(\bar{\zeta})}{\partial \bar{\zeta}} - U_{\text{eff}} \frac{\partial \bar{\Theta}(\bar{\zeta})}{\partial \bar{\zeta}} - U_{\text{eff}} \frac{n_w}{\varepsilon} \frac{\partial \Theta_s(\bar{\zeta})}{\partial \bar{\zeta}} = 0, \quad (29)$$

The effective propagation velocity U_{eff} can be determined by finding a relationship between $\bar{\Theta}(\zeta, \tau)$, $\Theta_b(\zeta, \tau)$, and $\Theta_s(\zeta, \tau)$ and by applying the boundary conditions very far upstream and downstream of the moving front to yield

$$U_{\text{eff}} = \left(1 + \frac{n_w}{\varepsilon(1 + \bar{K}_D)} \right)^{-1} U. \quad (30)$$

The front of bulk concentration $\Theta_b = 1$ will thus propagate at a velocity much inferior to the fluid velocity when $\varepsilon \ll 1$, which is normally the case. Moreover, it can be observed that U_{eff} is minimal when $\bar{K}_D \rightarrow 0$. This is to be expected since in this case, no ligand escapes the bed. The mathematical derivation of this result from the full transport equations is provided in Appendix A.2.

4.3. Wave profile determination for limiting cases

The analysis provided in the previous subsection only provides the propagation velocity but does not reveal anything about the profile of the kinematic wave inside the device. For arbitrary transport conditions, the exact shape of the wave front can only be determined numerically. However, two limiting cases exist whether the transport to the surface is diffusion or reaction limited. These wave profiles are necessary to predict the capture fraction in a device and are discussed below.

4.3.1. Fully diffusion-limited wave profiles

Under fully diffusion-limited conditions, the flux to the surface can be assumed constant throughout the device, as in Eq. (16). In the reference frame of the moving concentration

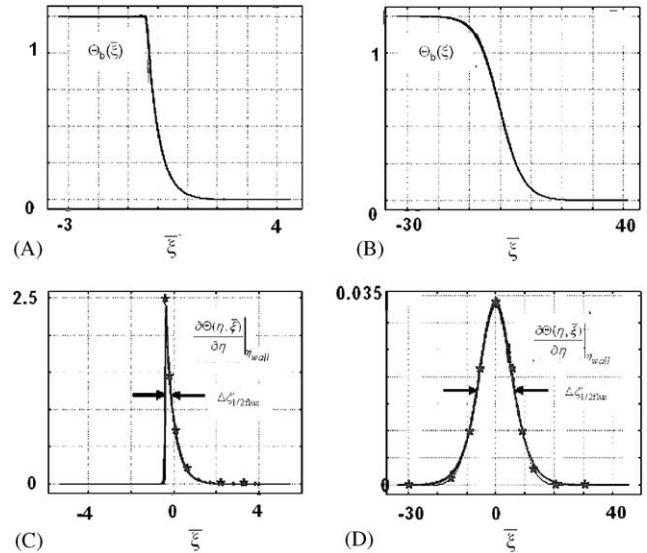


Fig. 5. Numerical simulation of bulk concentration and flux peak profiles for limiting transport situations ($n_w = 2$). (A–B) Fully reaction-limited case, $Da=0.14$, $\bar{K}_D=0$ (C–D). Fully mass transfer-limited case, $Da=100$, $\bar{K}_D=0$. The star-dotted curves in B and D represent the analytic models derived respectively in Eqs. (52) and (31).

front, the bulk concentration profile propagating inside the channel can therefore be approximated by a two piece-wise continuous profile:

$$\Theta_b(\bar{\zeta}) \sim \begin{cases} 1, & \bar{\zeta} < -\bar{\zeta}_{\text{shift}} \\ \Theta_b(\bar{\zeta}), & \bar{\zeta} > -\bar{\zeta}_{\text{shift}} \end{cases}, \quad (31)$$

where $\bar{\zeta}_{\text{shift}} \bar{t}_d = [\varepsilon(1 + \bar{K}_D)]^{-1} \bar{t}_d$ is the saturation time of the surface under diffusion-limited conditions, and Θ_b is given in Eq. (25). The peak shift $\bar{\zeta}_{\text{shift}}$ is explained by the time delay required for the surface to reach its steady state profile in the reference of the wave front before it starts propagating.

Numerical simulations presented in Fig. 5 confirm both the profile predicted by Eq. (31) and the peak shift $\bar{\zeta}_{\text{shift}}$ from the origin $\bar{\zeta} = 0$. The time dependent capture fraction of a bed of length L therefore becomes

$$f(t) \equiv 1 - \frac{\Theta_b(L)}{\Theta_b(0)} = \begin{cases} 1 - \Theta_b \left(\frac{L}{Pe h} - \frac{U_{\text{eff}} t}{U \bar{t}_d} + \frac{1}{\varepsilon(1 + \bar{K}_D)} \right) \\ \text{when } Da \gg 1 \end{cases} \quad (32)$$

4.3.2. Fully reaction-limited wave profiles

When the transport is fully reaction-limited, the concentration profile resembles one found in chromatography columns under continuous sample feed (Cazes and Scott, 2002). The wave front can be accurately approximated by a complementary error function (Abramowitz and Stegun, 1970) of the form

$$\Theta_b = \frac{1}{2} \text{erfc} \left(\frac{\bar{\zeta}}{\sqrt{2}\sigma} \right). \quad (33)$$

Where the standard deviation, representing the sharpness of the front (sharpest when $\sigma \rightarrow 0$), is given by

$$\sigma = \sqrt{\frac{2}{\pi}} \frac{1}{n_w \bar{k}_d / r (Da_{\text{eff}})} \quad (34)$$

Da_{eff} is the effective Damköhler number found at the point of half saturation of the surface, or

$$Da_{\text{eff}} = \frac{k_{\text{on}}(C_{s0} - C_{\text{c}q}/2)h}{D} = Da \frac{1/2 + \bar{K}_D}{1 + \bar{K}_D} \quad (35)$$

The details of the derivation are found in Appendix A.3. In Fig. 5B, the concentration profile found in Eq. (33) is confirmed by numerical simulations. The corresponding capture fraction by a bed of length L is therefore expressed by

$$f(\tau) = 1 - \frac{\Theta_b(L)}{\Theta_b(0)} = \frac{1}{2} \left(1 + \text{erf} \left\{ \frac{\zeta_L - U_{\text{eff}}\tau/U}{\sqrt{2}\sigma} \right\} \right), \quad \text{for } Da \ll 1. \quad (36)$$

In all cases, for these profiles to be observed, the condition of fully developed regime for ζ (see Figs. 2 and 4), must be respected.

4.4. Numerical simulation of the propagating front

A 2D model was created in FEMLAB to confirm the theoretical prediction of the propagation velocity of the concentration front and its general profile. The model is based on the general case of protein depletion from a solution in a binding assay performed in a narrow device in the fully developed region. To make the simulations physically relevant, the geometry, the experimental conditions, and the data on protein kinetics are taken from the literature (Table 2). The first simulation characterizes the passivation of channel walls using biotinylated bovine serum albumin (BSA) reacting with a wall coating of streptavidin in the conditions of a suspended microresonator. The parameters describing the model are, in this case, $Da = 0.14$, $Pe = 17$, $\varepsilon = 0.001$ and $\bar{K}_D \sim 0$ (Table 2, entry 2). The reaction occurs equally at both walls and is therefore symmetric. Modeling results are presented in Fig. 6 in terms of the bulk concentration $\Theta_b(\zeta, t)$, the normalized flux at the wall $\partial\Theta(\eta_w, \zeta, t)/\partial\eta$, and the surface concentration of bound BSA normalized to the total number of binding sites $\Theta_s(\zeta, t)$. The time scale chosen is from 100 to 2000 s where each curves is taken at a 50 s interval. In each of these curves, the time scale $\bar{t}_{\text{sat}} = (k_{\text{on}}C_0 + k_{\text{off}})^{-1} \sim 85$ s appears to be the time necessary for the wave to enter its self-propagating steady state (see discussion section).

In Fig. 6C, the emphasis is on early times (< 0.15 s) to capture the development of the flow on the time scale of diffusion across the channel height. In this time frame, the steady state value of the bulk concentration in the absence of surface saturation is also plotted (Fig. 6A, line with star

markers). The approximation is in agreement with the numerical model when a few diffusion time scales have elapsed (Section 3.5.2).

A similar analysis is provided in Fig. 7 for the case of affinity capture at the bottom wall of a 50- μm thick microfluidic channel. Given the larger diffusive time scale due to the increased channel thickness, the fully developed region will be reached at much higher length scales in this simulation. Indeed, to obtain this effect, the length of the capture bed would have to be of at least $L = 1$ cm ($\zeta \sim 0.7 \gg \zeta_{\text{crit}}$) instead of 0.1 mm as presented in the original BIACORE experiment (Catimel et al., 1997). In such a device, a ζ value of 5 corresponds to a length $L = 7.5$ cm. The simulation parameters for this particular application are then defined by $Da = 10$, $Pe = 335$, $\varepsilon = 0.07$ and $\bar{K}_D = 0.14$ (Table 2, entry 1). The reaction takes place only on one side wall in this case.

In both cases, if the transport of the solution above the reactive surfaces can indeed be characterized using an expression depending only on ε and \bar{K}_D , as derived in Eq. (32), all the time lines should merge into the same curve, representing the shape of the wave front, when they are presented in the reference frame of the propagating wave. To illustrate this behavior, the data is presented again with the variable change introduced in Eq. (28). Results are presented in Figs. 6C'–E' and 7C'–E'. They clearly indicate such a convergence after long enough times after the analyte has entered the channel.

5. Discussion

In microfluidics, most analyses assume that at high enough flow rates, a mass transfer boundary layer will exist in the device and that the models developed for the kinetic analysis of the Biacore sensor will apply. This is not always the case. As the channels become thinner, depletion from the bulk becomes important and the “entrance region” assumption can no longer be used. Inspection of Fig. 2 indicates that the model breaks down much before $\zeta = 1$. By plotting the absolute error of the bulk concentration for the fully numerical model versus the existing asymptotic solution, a model-selection criterion, i.e., a critical value of ζ above which the fully developed model provided a better approximation than the entrance model, arose naturally. The critical values are $\zeta_{\text{crit}} = 0.06$ and $\zeta_{\text{crit}} = 0.22$ for the symmetric and asymmetric reactions, respectively. This transition physically corresponds to the location along the length of the channel at which the mass transfer boundary layer is disrupted and the depletion in the bulk becomes significant. Therefore, the validity of the entrance region models developed for most real-time detection systems, including SPR systems, breaks down at ζ_{crit} .

Reducing the channel height also drives the transport towards the reaction-limited or even convection-limited regimes. The reaction-limited regime is captured in the

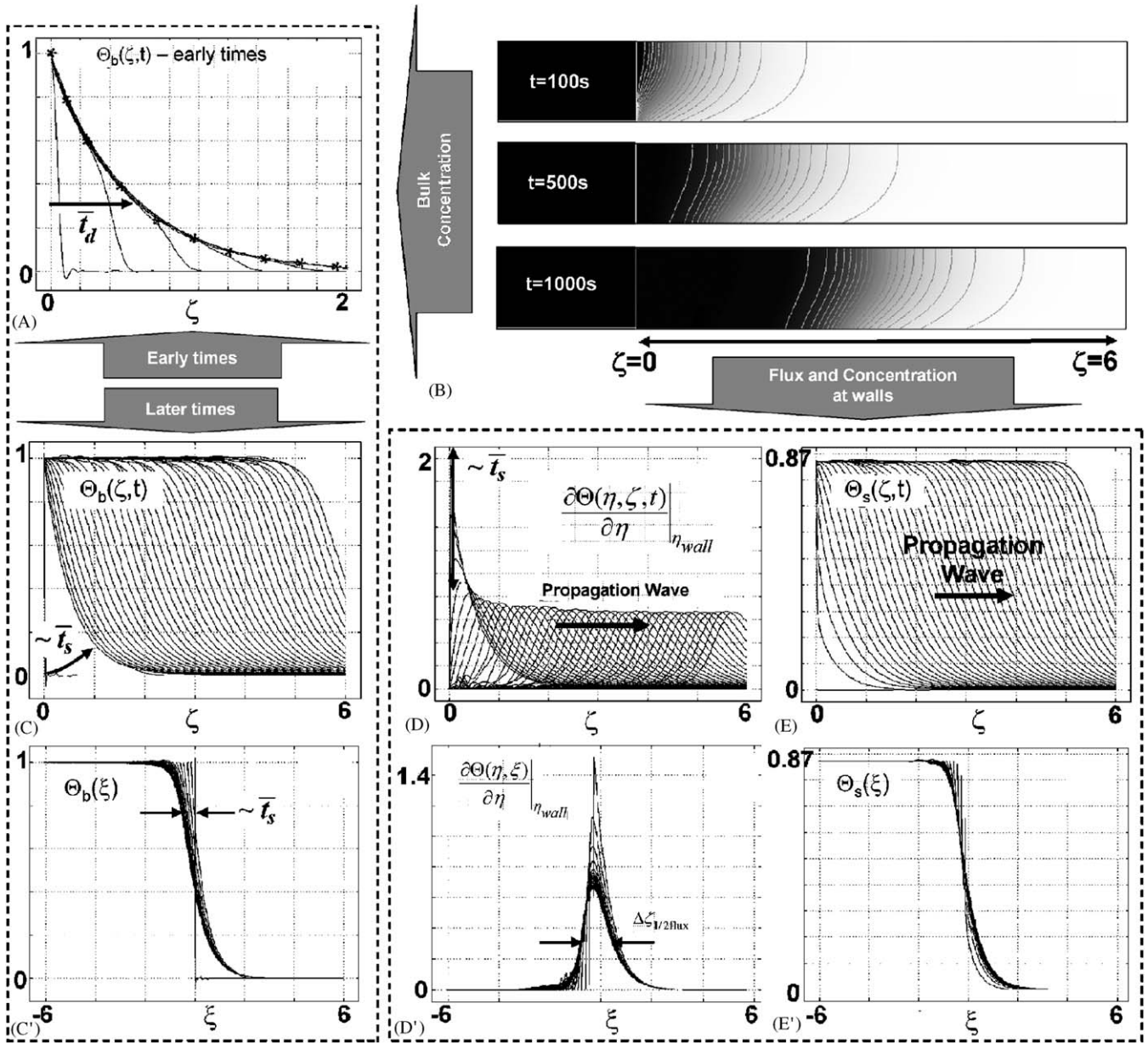


Fig. 6. Numerical simulation of flow of biotinylated bovine serum albumin (BSA) between streptavidin-coated walls. The geometry and experimental conditions are taken to simulate the suspended microresonator. (A) Bulk concentration profile for times ranging from 0 to 0.15 s ($\Delta t = 0.005$ s). The star-dotted line is a fit of the fully developed model for $Da = 0.14$ ($n_w \bar{k}_d / r = 0.27$). (B) FEMLAB simulations of flow for three different time points: 100 s (about the saturation time scale), 500 and 1000 s (above saturation time scale and in the propagation wave regime). The gray lines represent concentration isotherms. (C) Bulk concentration $\Theta_b(\zeta, t)$ as a function of ζ for times ranging from 50 to 2000 s ($\Delta t = 50$ s). (D) Normalized flux at the walls for a time range identical to A. (E) Normalized surface concentration of bound BSA (with respect to the total number of binding sites). Time range identical to A. (C'–E') Transport simulation in the reference frame of the propagation wave of velocity U_{eff} , where $U_{\text{eff}}/U = 5 \times 10^{-4}$. The various time lines converging to a same value after a few time scales $\bar{t}_{\text{sat}} = (k_{\text{on}} C_0 + k_{\text{off}})^{-1}$ illustrate clearly the development of a kinematic wave.

Damköhler number. Since $Da \equiv k_{\text{on}} C_{s,0} h / D$ for bimolecular surface reactions, as the channel height increases, Da will decrease correspondingly, to a point where the mass transfer will become fully reaction-limited for thin enough structures. However, the reaction can still become limited by convective transport ($\zeta Da \gg 1$) for small channel height since the convection/reaction number $\zeta Da \propto h^{-1}$.

The two examples modeled and presented in the results section are used to demonstrate the existence of the convection-limited regimes. Though they are of different lengths, channel height and kinetic properties, both fulfill the criterion $\zeta Da \gg 1$. Further physical insights can be gained from considering the five time scales present in this transport problem (diffusion \bar{t}_d , reaction \bar{t}_r ,

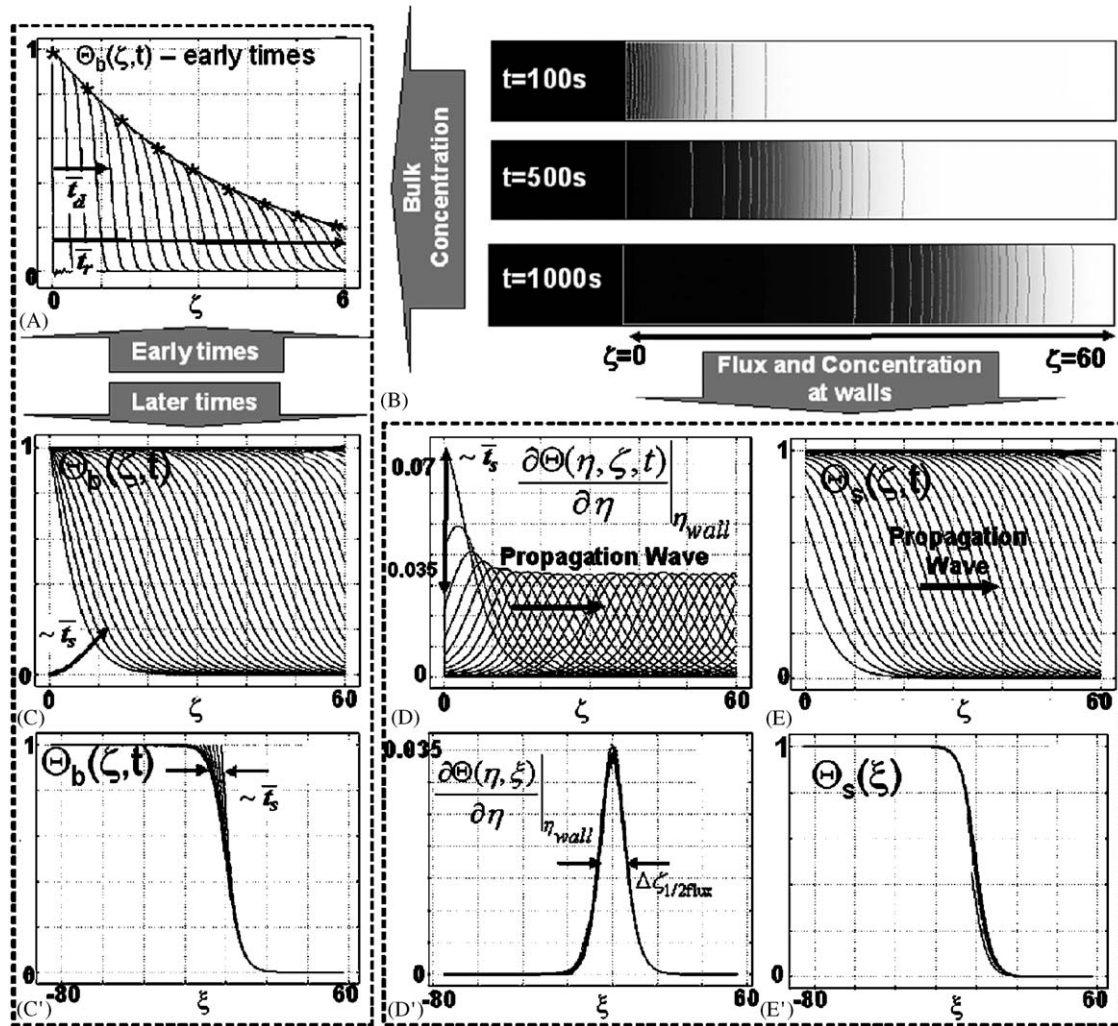


Fig. 7. Numerical simulation of flow of antigens (A33 protein) in a 50- μm thick channel in the fully developed regime. The lower wall is coated with corresponding antibody (asymmetric reaction). (A) Normalized bulk concentration $\Theta_b(\zeta, t)$ as a function of the diffusive/convective length ζ for early time points ($t = [0, 50]$) by steps of 10 s. The star-dotted line is a fit of the fully developed model for $Da = 10$ ($n_w k_d/r = 1.99$). (B) FEMLABTM simulation of flow for three different time points: 100, 500 and 1000 s. The gray lines represent concentration isotherms. (C) $\Theta_b(\zeta, t)$ vs ζ for time points in the propagation wave regime ($t = [0, 2000]$) by steps of 50 s. (D) Normalized flux at the antibody bed (same time points as (C)). (E) Normalized surface concentration of bound antigen. (C'–E') Transport simulation in the reference frame of the propagating front, where $U_{\text{eff}}/U = 0.074$.

convection \bar{t}_c , saturation \bar{t}_{sat} , and propagation \bar{t}_p . For the convection-limited (or wave) regime to occur, both the time taken for the analyte to diffuse across the channel (\bar{t}_d) and the time for it to react at the surface (\bar{t}_r) must be smaller than the time for the analyte to exit the reactive region (\bar{t}_p). No restriction is required on the relationship between \bar{t}_d and \bar{t}_r . Consequently, any Da can yield a convection-limited regime.

In the case of reaction in the suspended microresonator (Burg and Manalis, 2003), the diffusion time scale $\bar{t}_d = h^2/D \sim 20$ ms is the shortest of all and represents the time scale after which steady state is reached in the bulk and, therefore, the Graetz formulation of the problem can be used (Fig. 6A). The second time scale, $\bar{t}_r = (k_{\text{on}} C_{s0}/h)^{-1} = 0.12$ s, is still much smaller than the convection time scale $\bar{t}_c =$

$L/U = 1$ s, such that $\bar{t}_d \ll \bar{t}_r \ll \bar{t}_c$. The saturation time constant $\bar{t}_{\text{sat}} = (k_{\text{on}} C_0 + k_{\text{off}})^{-1} \sim 85$ s shows how quickly the propagation wave will develop throughout the device. Since we are in the convection-limited regime, the propagation time constant of the wave front is physically meaningful and can be calculated to be $\bar{t}_p = L/U_{\text{eff}} \sim 1530$ s. The ratio $\bar{t}_p/\bar{t}_c = U/U_{\text{eff}}$ indicates by how much the flow of analytes is retarded compared to the fluid flow. This ratio is analogous to the number of theoretical plates used in chromatography to determine a column's separation efficiency (see Appendix A.2). In this case, the retardation factor is 1530 times. In other words, while the fluid will take 1 s to traverse the reactive region, we predict that the analyte will propagate through the channel in 24 min given the values of ε and \bar{K}_D provided. The modeling results are presented

(Fig. 6C'–E') in the reference frame of the bulk solution propagating at velocity U_{eff} by using the change of variable introduced in Eq. (28). The quick convergence of the lines into one proves the accuracy of the approximation on U_{eff} made in Eq. (30).

The on-chip immunoassay described in Fig. 7 can be analyzed in the same fashion. The various time scales in this case are $\bar{t}_d = 25$ s, $\bar{t}_r = 3$ s (now transport to surface is diffusion-limited), and $\bar{t}_c = 112$ s. Though the propagation time scale \bar{t}_c is much larger in this second case, the retardation factor, $U/U_{\text{eff}} = 13.5$ is 113 times smaller in this case. Thus the wave front travels faster in the immunoassay than in the resonator, even though the fluid velocity is higher in the latter. This behavior can be explained by the lower adsorption capacity (higher ϵ), the lower equilibrium capture fraction (87% instead of 100%), and the presence of only one reactive wall in the former case (Fig. 7).

In the perfectly convection-limited case, the propagating front is a step function between a region where $\Theta_b(z < U_{\text{eff}}t) = 1$ and $\Theta_b(z > U_{\text{eff}}t) = 0$. However, operating in nonideal conditions, the front of concentration $\Theta_b = 1$ will be preceded by a region where the surface is partially saturated. Thus the scaling of Eq. (25) implies that a concentration decay length scale $\zeta_p \sim (n_w \bar{k}_{d/r})^{-1}$ will be perturbed during the formation of the wave. From this diffusive/convective length scale, it is possible to extract the propagation length scale required before the wave is fully formed

$$l_p \sim \frac{U \bar{t}_d}{n_w \bar{k}_{d/r}}, \quad (37)$$

For instance, in the structure analyzed in Fig. 6, $n_w \bar{k}_{d/r}(Da = 0.14) = 0.27$, $U = 2$ mm/s and $\bar{t}_d = 0.02$ s, which yields $l_p \sim 0.2$ mm (10% of the channel length).

Once the wave profile has reached steady state, the same scale can be used to determine the length of the partially saturated moving front. Indeed, when $\bar{t}_r \ll \bar{t}_d$ (or $Da \gg 1$) as in Fig. 5B, the flux curves are exponential in nature and their full width at half maximum (FWHM) becomes

$$\Delta \zeta_{1/2 \text{ flux}} \sim \frac{2 \ln 2}{n_w \bar{k}_{d/r}(Da)} = \frac{1.39}{n_w \bar{k}_{d/r}(Da)}. \quad (38)$$

The case of the immunoassay falls in that category ($Da = 10$), and $n_w \bar{k}_{d/r}(Da) = 1.99$ (from Fig. 3), $U = 0.67$ mm/s and $\bar{t}_d = 25$ s, which yields $l_p \sim 8.3$ mm and $\Delta \zeta_{1/2 \text{ flux}} \sim 1.39/k_{d/r}(Da) = 0.82$.

However, when $\bar{t}_d \ll \bar{t}_r$ (or $Da \ll 1$) the flux curves are Gaussian in shape and their FWHM is therefore approximated by

$$\Delta \zeta_{1/2 \text{ flux}} \approx 2\sigma\sqrt{2 \ln 2} = \frac{1.88}{n_w \bar{k}_{d/r}(Da_{\text{eff}})}. \quad (39)$$

Thus for the width at half maximum of the flux peak in the resonator ($Da = 0.14$), we obtain $\Delta \zeta_{1/2 \text{ flux}} = 1.88/\bar{k}_{d/r}(Da/2) = 13.7$.

In all cases, for a wave to be observed, the condition on the reaction zone length $L \gg l_p$ must be respected. Given also that $l_p \propto h^2$, a wave front is much less likely to appear in thicker microfluidic channels. As in the case of capillary chromatography, when the normalized dissociation constant \bar{K}_D is of order one or larger asymmetric peaks appear in a separation process (Scott, 1992). Under these circumstances, the chromatographic analysis becomes much more difficult.

6. Conclusion

Transport problems involving flow through devices and surface capture abound in the field of microfluidics. It can be difficult to select the appropriate model to characterize device performance as devices vary greatly in geometries and operation ranges. In many applications, it is not possible (or simply not desirable) to operate under conditions that yield a mass transfer boundary layer. This contribution establishes the limits of the entrance region models developed for SPR (Biacore) analysis. Through fully numerical simulations and analysis of the classical transport equations, the intervals of validity of these models are established. Most importantly, the analyses and modeling in this paper focus on fully characterizing transport to surfaces in the absence of boundary layer and proposes a simple approach to obtain the diffusion/reaction mass transfer coefficient $\bar{k}_{d/r}(Da)$. Application of these coefficients allows accurate mapping of the bulk and surface concentrations along the channel and helps determine the expected time for a surface to saturate. The formation of a moving concentration front in long channels is also investigated and its propagation velocity is linked directly to common experimental parameters. Finally, a few examples from the microfluidics literature provide concrete examples of the use of the models.

As the field of total biochemical analysis evolves, fluidic modules are bound to be integrated on a very large scale, both in series and in parallel, and analysis times will need to be controlled carefully. Saturation time scales and capture fractions in flow through reactions will be important parameters to optimize. Moreover, devices will tend to shrink in size to yield faster analysis times and more portability, but at the same time, will render boundary layer models useless as the length scale of these layers would be significantly larger than the channels themselves. This study represents a start towards systematizing the existing knowledge and identifying the key parameters to consider when designing microfluidics-based systems.

Notation

C	concentration
D	diffusivity
Da	Damköhler number (surface-bimolecular)
f	capture fraction
h	channel height
i	index variable
k	rate constant
K	equilibrium constant
l	characteristic length
L	length of reactive zone
M	Kummer Function
n	number
N	mass flux
Pe	Péclet number
Q	flow rate
R	reaction rate
Sh	Sherwood number
t	time
u	normal unit vector
U	average fluid velocity
v	velocity
w	channel width
x	height position variable
z	axial position variable

Greek letters

δ	boundary layer thickness
ε	volume-to-surface concentration ratio
ζ	convective/diffusive length scale
η	normalized height
λ	eigenvalue
ξ	moving front variable
σ	standard deviation
τ	normalized time
Θ	normalized concentration

Superscripts/subscripts

0	initial
asym	asymmetric
b	bulk
c	convection
crit	critical
d	diffusion
d/r	diffusion/reaction
D	dissociation
eq	equilibrium
eff	effective
E	entrance
FD	fully developed
L	at position $z = L$
off	reverse (to bulk)
on	forward (to surface)
p	propagation

r	reaction
s	surface
sat	saturation
sym	symmetric
v	volume
w	wall

Acknowledgements

The authors would like to thank Prof. William M. Deen for helpful discussions and comments, Thomas Burg for providing data on the microresonator experiments and Prof. Peter K. Sorger's group for general collaboration on the biology. This work has been supported by the National Institute of Health (PSO-GM068762). T.G. thanks the National Science and Engineering Research Council of Canada (NSERC) and the Fonds de Recherche sur la Nature et les Technologies du Québec (NATEQ) for financial support.

Appendix A. Analytic supplement*A.1. Algebraic proof of the faster convergence of transport coefficients at lower Damköhler numbers*

The proof is made by showing that the higher order contributions to the transport coefficients are given a lesser weight (coefficients $A(Da)_i$) in the sum as Da decreases. To do so, the generalized reaction/diffusion transport coefficient is expanded using Eq. (13) and the eigenfunction expansion found in Table 3 to give

$$\bar{k}_{d/r}(Da, \zeta) = \frac{1}{n_w} \frac{\sum_{i=1}^{\infty} A(Da)_i \frac{\lambda_i^2(Da)}{6} \exp\left(-\frac{\lambda_i^2(Da)}{6} \zeta\right)}{\sum_{i=1}^{\infty} A(Da)_i \exp\left(-\frac{\lambda_i^2(Da)}{6} \zeta\right)}, \quad (40)$$

when $\zeta \rightarrow 0$ and $Da \rightarrow \infty$, Eq. (40) slowly converges to the value of the entrance region Sherwood number Sh_E found in Eq. (14). Since $\lambda_{i+1}^2/\lambda_1^2 \approx i^2$, all terms but the first ones can be neglected for large ζ . Keeping the first two terms of the expansion, the order of magnitude of the error on $\bar{k}_{d/r}(Da, \zeta)$ will be determined by the ratio of the two first expansion coefficients A_2/A_1 at $\zeta = 0$, assumed to be small (yet much larger than $A_{i>2}/A_1$):

$$\begin{aligned} \bar{k}_{d/r}(Da, \zeta = 0) &\approx \frac{\lambda_1^2(Da)}{6} \left(\frac{1 + \frac{A_2 \lambda_2^2(Da)}{A_1 \lambda_1^2(Da)}}{1 + \frac{A_2}{A_1}} \right) \\ &\approx \frac{\lambda_1^2(Da)}{6} \left\{ 1 + \left(\frac{\lambda_2^2(Da)}{\lambda_1^2(Da)} - 1 \right) \frac{A_2}{A_1} \right. \\ &\quad \left. + O\left(\frac{A_2^2}{A_1^2}\right) \right\}, \quad (41) \end{aligned}$$

where the leading order corresponds to the relative error on $\bar{k}_{d/r}(Da)$

$$\text{err}(\%) \sim \left(\frac{\lambda_2^2(Da)}{\lambda_1^2(Da)} - 1 \right) \frac{A_2}{A_1}. \quad (42)$$

From Eq. (40), we observe that the error on $\bar{k}_{d/r}(Da, \zeta)$ is maximum at $\zeta = 0$, implying that the error calculated in Eq. (42) represents an upper bound. The error on $\bar{k}_{d/r}(Da)$ is computed and compared in Table A.1 for $Da \rightarrow \infty$ and $Da = 1$, and for both symmetric and asymmetric reactions. It shows that the first term approximation becomes even more appropriate at smaller Damköhler numbers, as the first expansion coefficient $A(Da)_1$ will tend to 1, while A_2/A_1 decreases.

A.2. Development and calculation of the propagation velocity of a kinematic concentration wave front

After several diffusion or reaction time scales have elapsed, whichever the longest, the bulk concentration profile, in the reference frame of the propagating wave front, will reach a steady-state due the constant adsorption along the walls. The velocity-averaged and cross-section-averaged concentration will become the same, and $\bar{\Theta}(\zeta, \tau) = \Theta_b(\zeta, \tau)$ can be assumed valid at all time $t \gg \bar{t}_d$. However, this simplification is not required to obtain the general result for the propagation velocity.

The propagation wave aspect appears when the equations are expressed with respect to the reference frame moving at a velocity U_{eff} , at which the concentration profile propagates once it has reached steady state. This approximation is valid for times for ζ sufficiently large and for $t \gg (k_{\text{on}}C_0 + k_{\text{off}})^{-1}$ the saturation time scale at the surface. This velocity is now unknown, but can be determined by first using the change of variable

$$\xi = z - U_{\text{eff}}t, \quad (43)$$

in such a way that the solution can be represented by an ordinary differential equation with dependent variables of the form

$$\Theta(z, t) = \Theta(\xi). \quad (44)$$

These satisfy the new boundary conditions

$$\begin{aligned} \Theta_b = \bar{\Theta} = 1, \quad \Theta_s = \frac{1}{1 + \bar{K}_D}, \\ \frac{d\Theta_b}{d\xi} = \frac{d\bar{\Theta}}{d\xi} = \frac{d\Theta_s}{d\xi} = 0, \quad \text{as } \xi \rightarrow -\infty, \end{aligned} \quad (45a)$$

$$\begin{aligned} \Theta_b = \bar{\Theta} = \Theta_s = 0, \quad \frac{d\Theta_b}{d\xi} = \frac{d\bar{\Theta}}{d\xi} = \frac{d\Theta_s}{d\xi} = 0, \\ \text{as } \xi \rightarrow \infty. \end{aligned} \quad (45b)$$

In a first order ODE, these conditions cannot be satisfied all at once. However, if the problem exhibits a kinematic wave behavior, then Eqs. (43) and (44) are appropriate. The solution found is a shock, exhibiting a discontinuity. An extensive study of their behavior and applications is provided by Rhee and Amundson (Rhee et al., 1989).

With the new change of variable, and expressing ζ and τ in terms of z and t , the flux balance in Eq. (27) becomes

$$\begin{aligned} N_{\text{tot}}(\xi) = U \frac{d\Theta_b(\xi)}{d\xi} - U_{\text{eff}} \frac{d\bar{\Theta}(\xi)}{d\xi} \\ - n_w \frac{U_{\text{eff}}}{\varepsilon} \frac{d\Theta_s(\xi)}{d\xi} = 0, \end{aligned} \quad (46)$$

giving a differential expression of $\Theta_s(\zeta, t)$ as a function of $\Theta_b(\xi)$ and $\bar{\Theta}(\xi)$.

When one is not interested in knowing the exact profile of the propagation wave (i.e., $\Theta_b(\xi)$ and $\Theta_s(\xi)$), but only the velocity of the resulting wave, it can be readily obtained by integrating Eq. (46) over the whole domain ($\xi = [-\infty, \infty]$). The integration gives

$$\begin{aligned} \int_{-\infty}^{\infty} N_{\text{tot}}(\xi) d\xi = n_w \frac{U_{\text{eff}}}{\varepsilon} [\Theta_s(\xi)]_{-\infty}^{\infty} - U [\Theta_b(\xi)]_{-\infty}^{\infty} \\ - U_{\text{eff}} [\bar{\Theta}(\xi)]_{-\infty}^{\infty} = 0. \end{aligned} \quad (47)$$

Using the boundary conditions expressed in Eq. (45a), the result can be rearranged to obtain the key result found in Eq. (32). To pursue an analogy with chromatography theory, the ratio

$$\frac{U}{U_{\text{eff}}} = 1 + \frac{n_w}{\varepsilon} (1 + \bar{K}_D), \quad (48)$$

represents here the number of theoretical plates in a capillary column inside which bimolecular surface saturation is permitted. However, the standard capillary columns assume purely first order kinetics and further simplify the analysis by assuming that the walls never saturate (Scott, 1992), the standard definition of the number of theoretical plates is defined with K_D replacing \bar{K}_D in Eq. (48), and assuming the surface never saturates.

A.3. Analytic characterization of the wave front and flux peaks under reaction-limited transport

Contrary to the chromatography models, where no surface saturation is assumed, the problem addressed here is highly nonlinear. As a result, the exact expression of the curve shape can only be found through numerical simulation. However, by assuming pseudo steady state in the concentration curves (Figs. 6C', 5E' and Figs. 7C', 6E'), the total flux (or the slope of the concentration curve) near the inflection point can be approximated accounting for the

Table 5
Numerical values of eigenvalues and eigenfunction expansion coefficients for selected Damköhler numbers

	$[a_1, a_2]$	$[A_1, A_2]$	$[\lambda_1, \lambda_2]$	$\bar{k}_{d/r}(Da)$	Error (%)
Symmetric, $Da \rightarrow \infty$	[1.20083, −0.299161, 0.160826, −0.107437, 0.0796461]	[0.910352, 0.0531425, 0.0152789, 6.80881E−3, 3.73980E−3]	[6.72638, 22.6794, 38.6730, 54.6706, 70.6695]	3.77035	60
Symmetric, $Da \rightarrow 1$	[1.05440, −0.0702248, 0.0231974, −0.0116351, 7.04946E−3]	[0.996534, 3.00272E−3, 3.20666E−4, 8.02227E−5, 2.93823E−5]	[3.10203, 17.9834, 33.7725, 49.6771, 65.6209]	0.801883	10
Asymmetric, $Da \rightarrow \infty$	[1.24843, −0.383224, 0.226317, −0.160582, −0.124437]	[0.895561, 0.0604998, 0.0180406, 8.17716E−3, 4.53590E−3]	[3.81867, 11.8972, 19.9241, 27.9383, 35.9473]	2.43036	59
Asymmetric, $Da \rightarrow 1$	[1.80850, −0.0177920, 0.0897772, −2.03146E−3, 0.0321345]	[0.992098, 6.67512E−3, 8.26276E−4, 2.19425E−4, 8.30061E−5]	[2.08371, 9.67057, 17.5723, 25.5244, 33.4952]	0.723641	14

The reaction/diffusion transport coefficient and the maximum relative error committed by using the fully developed region asymptotic model instead of the entrance region model is also provided.

partially saturated surface

$$\left. \frac{\partial \Theta_b}{\partial \bar{\xi}} \right|_{\bar{\xi}=0} = -n_w \bar{k}_{d/r}(Da_{\text{eff}}) \Theta_b|_{\bar{\xi}=0} = -n_w \bar{k}_{d/r}(Da_{\text{eff}})/2. \quad (49)$$

We note that $\Theta_b = 1/2$ at the inflection point.

We also observe that Figs. 6C', 5E' and Figs. 6C', 6E', the curves representing the bulk and surface concentration in the referential of the wave front behave like the complementary error function (Abramowitz and Stegun, 1970)

$$\frac{1}{2} \text{erfc} \left(\frac{\bar{\xi}}{(\sqrt{2} \cdot \sigma)} \right) = \frac{1}{2} \sqrt{\frac{2}{\pi \sigma^2}} \int_{\bar{\xi}}^{\infty} \exp\{-\bar{\xi}^2/2\sigma^2\} d\bar{\xi} \approx \frac{1}{2} \left\{ 1 - \sqrt{\frac{2}{\pi \sigma^2}} \bar{\xi} \right\}, \quad \text{if } \bar{\xi} \rightarrow 0. \quad (50)$$

By comparing the result in Eq. (49) with the slope of the complementary error function near $\bar{\xi}=0$, the effective value of σ can be inferred and used to estimate the shape of the wave front.

$$-\frac{1}{2} \sqrt{\frac{2}{\pi \sigma^2}} = -n_w \bar{k}_{d/r}(Da_{\text{eff}})/2 \Rightarrow \sigma = \sqrt{\frac{2}{\pi}} \frac{1}{n_w \bar{k}_{d/r}(Da_{\text{eff}})}, \quad (51)$$

when $\sigma \ll 1$, the function resembles a step function and the wave front becomes ideal.

Finally, the total flux to the surface (Figs. 6D' and 7D') being the derivative of the concentration, it is thus normal

to observe that the flux peaks are approximately Gaussian. On a per surface basis, the flux becomes

$$\frac{1}{n_w} \sqrt{\frac{2}{\pi \sigma^2}} \exp\{-\bar{\xi}^2/2\sigma^2\} = \frac{\bar{k}_{d/r}(Da_{\text{eff}})}{2} \exp\left\{-\frac{\pi}{4} [n_w \bar{k}_{d/r}(Da_{\text{eff}}) \bar{\xi}]^2\right\}. \quad (52)$$

This expression is very accurate near the inflection point $\bar{\xi}=0$ for reaction with small \bar{K}_D . Thus the Gaussian peak model can be used with confidence to predict the head size of the wave front for $\bar{K}_D \ll 1$ and $Da \ll 1$, while it only becomes an approximation at larger \bar{K}_D 's and $Da \sim 1$ since Eq. (49) cannot take dissociation rates into account. For $Da \gg 1$, Eq. (31) (and its derivative for the flux) must be used.

References

- Abramowitz, M., Stegun, I.A., 1970. Handbook of Mathematical Functions. Dover Publications, New York.
- Auroux, P.A., Iossifidis, D., Reyes, D.R., Manz, A., 2002. Micro total analysis systems. 2. Analytical standard operations and applications. Analytical Chemistry 74 (12), 2637–2652.
- Bernard, A., Michel, B., Delamarche, E., 2001. Micromosaic immunoassays. Analytical Chemistry 73 (1), 8–12.
- Bird, R.B., Stewart, W.E., Lightfoot, E.N., 2002. Transport Phenomena. second ed. Wiley, New York.
- Brockman, J.M., Nelson, B.P., Corn, R.M., 2000. Surface plasmon resonance imaging measurements of ultrathin organic films. Annual Review of Physical Chemistry 51, 41–63.
- Brown, G.M., 1960. Heat of mass transfer in a fluid in laminar flow in a circular or flat conduit. A.I.Ch.E. Journal 6 (2), 179–183.
- Burg, T.P., 2004. Personal communication.

- Burg, T.P., Manalis, S.R., 2003. Suspended microchannel resonators for biomolecular detection. *Applied Physics Letters* 83 (13), 2698–2700.
- Catimel, B., Nerrie, M., Lee, F.T., Scott, A.M., Ritter, G., Welt, S., Old, L.J., Burgess, A.W., Nice, E.C., 1997. Kinetic analysis of the interaction between the monoclonal antibody A33 and its colonic epithelial antigen by the use of an optical biosensor—A comparison of immobilisation strategies. *Journal of Chromatography A* 776 (1), 15–30.
- Cazes, J., Scott, R.P.W., 2002. *Chromatography Theory*. Marcel Dekker, New York.
- Christensen, L.L.H., 1997. Theoretical analysis of protein concentration determination using biosensor technology under conditions of partial mass transport limitation. *Analytical Biochemistry* 249 (2), 153–164.
- Craighead, H.G., 2000. Nanoelectromechanical systems. *Science* 290 (5496), 1532–1535.
- de Mas, N., Gunther, A., Schmidt, M.A., Jensen, K.F., 2003. Microfabricated multiphase reactors for the selective direct fluorination of aromatics. *Industrial & Engineering Chemistry Research* 42 (4), 698–710.
- Deen, W.M., 1998. *Analysis of Transport Phenomena*. Oxford University Press, New York, Oxford.
- Elowitz, M.B., Surette, M.G., Wolf, P.E., Stock, J.B., Leibler, S., 1999. Protein mobility in the cytoplasm of *Escherichia coli*. *Journal of Bacteriology* 181 (1), 197–203.
- Fan, Z.H., Harrison, D.J., 1994. Micromachining of capillary electrophoresis injectors and separators on glass chips and evaluation of flow at capillary intersections. *Analytical Chemistry* 66 (1), 177–184.
- Glaser, R.W., 1993. Antigen–antibody binding and mass-transport by convection and diffusion to a surface—a 2-dimensional computer-model of binding and dissociation kinetics. *Analytical Biochemistry* 213 (1), 152–161.
- Goldstein, B., Coombs, D., He, X.Y., Pineda, A.R., Wofsy, C., 1999. The influence of transport on the kinetics of binding to surface receptors: application to cells and BIAcore. *Journal of Molecular Recognition* 12 (5), 293–299.
- Green, R.J., Davies, M.C., Roberts, C.J., Tendler, S.J.B., 1999. Competitive protein adsorption as observed by surface plasmon resonance. *Biomaterials* 20 (4), 385–391.
- Happel, J., Brenner, H., 1965. *Low Reynolds Number Hydrodynamics*. Englewood Cliffs, N.J.
- Hsu, C.J., 1968. Exact solution to entry-region laminar heat transfer with axial conduction and the boundary condition of the third kind. *Chemical Engineering Science* 23, 457–468.
- Huang, W.H., Cheng, W., Zhang, Z., Pang, D.W., Wang, Z.L., Cheng, J.K., Cui, D.F., 2004. Transport, location, and quantal release monitoring of single cells on a microfluidic device. *Analytical Chemistry* 76 (2), 483–488.
- Lok, B.K., Cheng, Y.L., Robertson, C.R., 1983. Protein adsorption on crosslinked polydimethylsiloxane using total internal-reflection fluorescence. *Journal of Colloid and Interface Science* 91 (1), 104–116.
- Lu, H., Koo, L.Y., Wang, W.M., Lauffenburger, D.A., Griffith, L.G., Jensen, K.F., 2004. Microfluidic shear devices for quantitative analysis of cell adhesion. *Analytical Chemistry* 76 (18), 5257–5264.
- MacBeath, G., Schreiber, S.L., 2000. Printing proteins as microarrays for high-throughput function determination. *Science* 289 (5485), 1760–1763.
- Madou, M.J., 2002. *Fundamentals of Microfabrication: The Science of Miniaturization*. CRC Press, Boca Raton, FL.
- Malmqvist, M., 1993. Biospecific interaction analysis using biosensor technology. *Nature* 361 (6408), 186–187.
- Mason, T., Pineda, A.R., Wofsy, C., Goldstein, B., 1999. Effective rate models for the analysis of transport-dependent biosensor data. *Mathematical Biosciences* 159 (2), 123–144.
- Myszka, D.G., He, X., Dembo, M., Morton, T.A., Goldstein, B., 1998. Extending the range of rate constants available from BIAcore: Interpreting mass transport-influenced binding data. *Biophysical Journal* 75 (2), 583–594.
- Nielsen, U.B., Cardone, M.H., Sinskey, A.J., MacBeath, G., Sorger, P.K., 2003. Profiling receptor tyrosine kinase activation by using Ab microarrays. *Proceedings of the National Academy of Sciences of the United States of America* 100 (16), 9330–9335.
- Okahata, Y., Kawase, M., Niikura, K., Ohtake, F., Furusawa, H., Ebara, Y., 1998. Kinetic measurements of DNA hybridisation an oligonucleotide-immobilized 27-MHz quartz crystal microbalance. *Analytical Chemistry* 70 (7), 1288–1296.
- Papoutsakis, E., Ramkrishna, D., 1981. Conjugated Graetz problems. 1. General formalism and a class of solid–fluid problems. *Chemical Engineering Science* 36 (8), 1381–1391.
- Polzius, R., Diessel, E., Bier, F.F., Bilitewski, U., 1997. Real-time observation of affinity reactions using grating couplers: Determination of the detection limit and calculation of kinetic rate constants. *Analytical Biochemistry* 248 (2), 269–276.
- Rhee, H.Y., Aris, R., Amundson, N.R., 1989. *First-Order Partial Differential Equations*, vol. 1 and 2. Prentice Hall, New Jersey.
- Schuck, P., 1997. Use of surface plasmon resonance to probe the equilibrium and dynamic aspects of interactions between biological macromolecules. *Annual Review of Biophysics and Biomolecular Structure* 26, 541–566.
- Scott, R.P.W., 1992. *Liquid Chromatography Column Theory*. Wiley, New York.
- Shah, R.K., London, A.L., 1978. *Laminar flow forced convection in ducts*. Academic Press, New York.
- Stone, H.A., Kim, S., 2001. Microfluidics: basic issues, applications, and challenges. *A.I.Ch.E. Journal* 47 (6), 1250–1254.
- Stone, H.A., Stroock, A.D., Ajdari, A., 2004. Engineering flows in small devices: Microfluidics toward a lab-on-a-chip. *Annual Review of Fluid Mechanics* 36, 381–411.
- Thorsen, T., Maerkl, S.J., Quake, S.R., 2002. Microfluidic large-scale integration. *Science* 298 (5593), 580–584.
- Vijayendran, R.A., Leckband, D.E., 2001. A quantitative assessment of heterogeneity for surface-immobilized proteins. *Analytical Chemistry* 73 (3), 471–480.
- Wang, Y., Vaidya, B., Farquar, H.D., Stryjewski, W., Hammer, R.P., McCarley, R.L., Soper, S.A., Cheng, Y.W., Barany, F., 2003. Microarrays assembled in microfluidic chips fabricated from poly(methyl methacrylate) for the detection of low-abundant DNA mutations. *Analytical Chemistry* 75 (5), 1130–1140.
- Wofsy, C., Goldstein, B., 2002. Effective rate models for receptors distributed in a layer above a surface: Application to cells and biacore. *Biophysical Journal* 82 (4), 1743–1755.
- Yarmush, M.L., Patankar, D.B., Yarmush, D.M., 1996. An analysis of transport resistances in the operation of BIAcore(TM): implications for kinetic studies of biospecific interactions. *Molecular Immunology* 33 (15), 1203–1214.